Mon. Not. R. Astron. Soc. **397,** 172–189 (2009) doi:10.1111/j.1365-2966.2009.14961.x

AGN with strong forbidden high-ionization lines selected from the Sloan Digital Sky Survey

Jonathan M. Gelbord,★ James R. Mullaney★ and Martin J. Ward★

Department of Physics, Durham University, South Road, Durham DH1 3LE

Accepted 2009 April 23. Received 2009 April 23; in original form 2008 October 6

ABSTRACT

We have defined a sample of 63 active galactic nuclei with strong forbidden high-ionization line (FHIL) emission. These lines, with ionization potentials $\gtrsim$100 eV, respond to a portion of the spectrum that is often difficult to observe directly, thereby providing constraints on the extreme ultraviolet-soft X-ray continuum. The sources are selected from the Sloan Digital Sky Survey (SDSS) on the basis of their [Fe X]λ6374 Å emission, yielding one of the largest and the most homogeneous samples of FHIL-emitting galaxies. We fit a sequence of models to both FHILs ([Fe XI], [Fe X] and [Fe VII]) and lower ionization emission lines ([O III], [O I], Hα, [N II], [S II]) in the SDSS spectra. These data are combined with X-ray measurements from the *ROSAT* satellite, which are available for half of the sample. The correlations between these parameters are discussed for both the overall sample and subsets defined by spectroscopic classifications. The primary results are evidence that (1) the [Fe X] and [Fe XI] lines are photoionized and their strength is proportional to the continuum flux around 250 eV, (2) the FHIL-emitting clouds form a stratified outflow in which the [Fe X] and [Fe XI] source regions extend sufficiently close to the broad-line region that they are partially obscured in Seyfert 2s, whereas the [Fe VII] source region is more extended and is unaffected by obscuration, (3) narrow-lined Seyfert 1s (NLS1s) tend to have the strongest [Fe X] flux (relative to lower ionization lines) and (4) the most extreme [Fe X] ratios (such as [Fe X]/[O III] or [Fe X]/[Fe VII]) are found in the NLS1s with the narrowest broad lines and appear to be an optical-band indication of objects with strong X-ray soft excesses.

Key words: line: profiles – galaxies: active – galaxies: individual: KUG 1031+398, RBS 1249, SDSS J124134.25+442639.2 – quasars: emission lines – galaxies: Seyfert – X-rays: galaxies.

1 INTRODUCTION

The forbidden high-ionization emission lines (FHILs) have been known to exist in the optical spectra of Seyfert galaxies for more than 40 years (see Oke & Sargent 1968 for the earliest published discussion of the [Fe X] species in NGC 4151). Historically, the [Fe X] line and other highly ionized species have been referred to in the literature as 'coronal lines' because these species were first identified in the spectra of the solar corona. However, in this paper we will refer to them in terms of a specific physical property, i.e. as FHILs. We include in our definition of FHILs any forbidden line having an ionization potential (IP) $\gtrsim$ 100 eV.

These lines are of interest for a variety of reasons. They define the nature of a galaxy in which they are detected as an active galactic nucleus (AGN). This is because stellar spectra do not have sufficient high-energy photons (>100 eV) to produce such species at detectable levels. Although supernova remnants can exhibit FHILs, these are distinguishable from those in AGN based on other properties, such as their profiles and velocity shifts with respect to other emission lines of lower ionization. In AGN, the FHILs tend to be broader and sometimes blueshifted compared to the profiles of the other emission lines (Appenzeller & Öestreicher 1988; Erkens, Appenzeller & Wagner 1997). Despite being well studied, some fundamental questions are still not settled, such as whether the FHIL-emitting regions are powered by photoionization or collisional processes. Also, the location of the zone in which the bulk of their line flux is emitted is not well established, although in some cases it has been possible to spatially resolve the region (see Rodríguez-Ardila et al. 2006 for a recent study). Their velocity widths imply a possible origin in a region contiguous with the innermost zones of the classic narrow-line region (NLR), as defined by [O III]λ5007. This region can be spatially resolved to about

★E-mail: j.m.gelbord@durham.ac.uk (JMG); j.r.mullaney@durham.ac.uk (JRM); m.ward@durham.ac.uk (MJW)

10 parsecs for some nearby AGN (e.g. Kraemer, Schmitt & Crenshaw 2008), and extends out to hundreds of parsecs and even kiloparsecs in some cases (e.g. Bennert et al. 2006a,b). By comparison, the broad-line region (BLR) is spatially unresolved, but is inferred from emission line reverberation mapping to be less than about a light month for a Seyfert of typical luminosity (Peterson et al. 2004).

On size scales between the BLR and the innermost resolved NLR lies the putative dusty molecular torus. This is believed to be a parsec-scale structure, with an inner edge that depends on the dust sublimation radius and may lie just beyond the BLR (Barvainis 1987; Suganuma et al. 2006). Based on these generic components, it has been suggested that the innermost FHIL-emitting regions lie somewhere between just beyond the BLR and the dusty torus. In addition to these qualitative considerations, the physical conditions of the FHILs, such as the density and temperature of the emitting gas derived from modelling their line flux ratios, have led to claims of an association with the so-called X-ray warm absorber (Porquet et al. 1999). This is an X-ray component very commonly identified in the low-energy X-ray spectra of Seyfert 1s (Blustin et al. 2005). A consequence of these and other properties is that FHILs may be employed as diagnostics of outflows from the inner regions of the AGN, and may be a useful ingredient of wind models (Rodríguez-Ardila et al. 2006; Mullaney et al. 2009).

Unfortunately, a current limitation in the study of FHILs and their potential use as diagnostics of the inner line-emitting regions of AGN is that the samples available are quite small and heterogeneous, being limited to bright, relatively nearby AGN (De Robertis & Osterbrock 1984; Veilleux 1988; Erkens et al. 1997; Murayama & Taniguchi 1998, hereafter MT98; Nagao, Taniguchi & Murayama 2000, hereafter NTM00). In this paper, we introduce a new sample of significant size, constructed using the FHILs themselves as a selection criterion, the first time this technique has been employed. This larger sample will enable meaningful statistical tests to be performed on the FHILs and other properties of the AGN, and also to consider the relevance of AGN classifications, such as Seyfert 1, Seyfert 2 and narrow-line Seyfert 1 (Sy1, Sy2 and NLS1, respectively).

The sample selection is presented in Section 2. In Section 3, we describe the models and the fitting procedure applied to the optical data, and how we interpret both these models and X-ray count rates from *ROSAT*. The results of these analyses are characterized in Section 4. In Section 5, we consider the implications of these results. Our findings are summarized in Section 6.

We adopt cosmological parameters from *Wilkinson Microwave Anisotropy Probe* (*WMAP*; $H_0 = 71\ \mathrm{km\,s^{-1}\,Mpc^{-1}}$, $\Omega_\mathrm{M} = 0.27$ and $\Omega_\Lambda = 0.73$; Spergel et al. 2003). The wavelengths reported throughout this paper are those observed in air, not the vacuum wavelengths reported in the Sloan Digital Sky Survey (SDSS; York et al. 2000) catalogue. This is for consistency with the vast majority of previous literature on this subject. Reported errors for fitted parameters are $\pm1\sigma$ confidence intervals; when average properties of samples are discussed, we generally provide both the $\pm1\sigma$ confidence interval of the mean value and the rms scatter about the mean.

2 SAMPLE SELECTION

Our objective is to construct a sample of galaxies selected based on their strong FHIL emission. We do not make the a priori assumption that such emission will only be found in AGN. Because FHIL emission is relatively rare, we require a large spectroscopic survey from which to draw our sample. For this the SDSS is ideally suited, in that Data Release 6 (DR6; Adelman-McCarthy et al. 2008) provides uniform quality spectra for nearly 900 000 galaxies and AGN spanning more than two steradians (6860 deg^2).

The SDSS data processing pipeline (Stoughton et al. 2002) fits simple Gaussian models to a set of features in each spectrum, yielding a data base of line parametrizations that is readily searched. Unfortunately, this data base does not include any optical FHILs. However, it does include both lines of the [O I]λλ6300, 6364 doublet. [O I]λ6364 is close enough to [Fe X]λ6374 that the SDSS line model will represent a blend of these two features if this FHIL is present. In such cases, the pipeline models of the [O I] lines will neither share the same profile nor have a 3:1 flux ratio, as expected from atomic physics. Thus [Fe X]-emitting galaxies may be found by identifying SDSS spectra whose [O I]λ6364 models show evidence of contamination.

We construct a sample of candidate [Fe X]-emitting galaxies by applying the following selection criteria to the SDSS data base:

(i) identified as either a galaxy or a quasar by the SDSS spectroscopic pipeline (SPECCLASS = 2 or 3, respectively);

(ii) redshift <0.40 to ensure that Hα lies within the observed 3800–9200 Å wavelength range;

(iii) Hα Gaussian model width $\sigma < 50$ Å to minimize the contamination of [O I] by any broad Hα wings;[1]

(iv) [O I] doublet models with significance greater than 10σ in each line to ensure well-defined profiles;

(v) [O I]λ6364 line centroids shifted by $\geq$1.5 Å relative to [O I]λ6300 (in the emitted frame; equivalent to $>$1.0 SDSS spectral bin), which is indicative of [Fe X] blends.[2]

The resulting ∼200 candidates were then visually inspected to identify the highest quality sources and to eliminate spectra with obvious contamination around 6370 Å (sky subtraction artefacts or any unmodelled Hα components that introduce steep gradients). Sources were selected for the final sample that have one or more pieces of unambiguous corroborating evidence of FHIL emission: (1) a distinct emission feature near 6374 Å; (2) [O I] + [Fe X] blends significantly broader than [O I]λ6300; (3) [O I] doublet ratio inconsistent with 3 and/or (4) prominent Fe VIIλ6087 emission.

The final sample, consisting of 64 strong [Fe X]-emitting galaxies, is presented in Table 1. The columns are (1) ID number; (2) J2000.0 coordinates; (3) SDSS SPECCLASS value ('SC'; 2 = galaxy, 3 = quasar); (4) our spectral classification (see Section 3.2.5); (5) *r* magnitude integrated over a 3-arcsec diameter region (SDSS fibre magnitude); (6) redshift defined from the observed wavelengths of the [S II] doublet (see Section 3.2.2); (7) correction to recessional velocity due to difference between SDSS- and [S II]-defined z ($\mathrm{km\,s^{-1}}$; $\Delta v_\mathrm{corr} < 0$ if $z_\mathrm{SDSS} < z_\mathrm{[S\,II]}$); (8–10) SDSS [O I] model parameters that provide evidence of blended [Fe X]: (8) offset of [O I]λ6364 model centroid from expected position ($\Delta\lambda_\mathrm{[O\,I]6364} = \lambda_\mathrm{[O\,I]6364} - \lambda_\mathrm{[O\,I]6300} - 63.472$ Å, where wavelengths are measured in the emitted frame in Å), (9) difference in widths of [O I] doublet line models ($\Delta\mathrm{FWHM} = \mathrm{FWHM}_{6364} - \mathrm{FWHM}_{6300}$, in Å) and (10) flux ratio of [O I]λ6300/[O I]λ6364; and (11)

[1] We note that the single-Gaussian model used by the SDSS pipeline may not be fitted to the broadest Hα component, so contamination at [O I] is still a possibility.

[2] The [O I]λ6364 model centroid shift was used instead of criteria based upon either the line flux ratios or FWHM differences because it was found to be more robust. The alternative tests were more likely to produce a false positive in response to relatively low signal-to-noise ratio (S/N) data, local inaccuracies in the SDSS continuum models or Hα contamination.

Table 1. SDSS galaxies selected by [Fe X] emission (see Section 2 for column descriptions).

ID	RA ± Dec. (J2000.0)	SC	Class	r	$z_{[S\,II]}$	v_{corr}	$\Delta\lambda_{[O\,I]6364}$	ΔFWHM	[O I] ratio	Alternative IDs
1	00:18:52.47+01:07:58.5	2	S1.9	18.10	0.0640	−47	7. ± 2.	12. ± 4.	0.70 ± 0.09	
2	01:10:09.01–10:08:43.4	3	NLS1	17.60	0.0583	−66	3. ± 3.	15. ± 4.	0.57 ± 0.07	1WGA J0110.1−1008
3	02:33:01.24+00:25:15.0	2	S2	15.39	0.0224	19	4.3 ± 0.4	2.9 ± 1.0	0.80 ± 0.08	1WGA J0232.9+0025
4	07:31:26.69+45:22:17.5	3	S1.5	17.84	0.0921	−4	3. ± 4.	11. ± 6.	1.06 ± 0.13	
5	07:36:38.86+43:53:16.5	2	S2	17.96	0.1140	37	3.5 ± 1.3	8. ± 3.	1.55 ± 0.17	
6	07:36:50.08+39:19:55.2	2	S2	19.12	0.1163	−13	5.8 ± 1.8	13. ± 4.	0.98 ± 0.10	
7	08:07:07.18+36:14:00.5	2	S2	16.23	0.0324	−21	8.5 ± 1.0	19.0 ± 1.6	0.25 ± 0.03	IC 2227
8	08:11:53.16+41:48:20.0	2	S2	18.35	0.0999	−96	5.6 ± 0.7	1.6 ± 1.9	1.45 ± 0.14	
9	08:29:30.59+08:12:38.1	3	S1.0	17.24	0.1295	−95	6.5 ± 1.0	15. ± 3.	0.54 ± 0.05	
10	08:30:45.37+34:05:32.1	3	S1.5	16.66	0.0624	−39	5.0 ± 0.9	13. ± 2.	0.89 ± 0.09	
11	08:30:45.41+45:02:35.9	3	S1.0	17.84	0.1825	−49	3. ± 6.	16. ± 5.	0.22 ± 0.02	
12	08:36:58.91+44:26:02.4	3	S1.0	15.71	0.2544	15	2.0 ± 1.2	10.6 ± 1.3	0.60 ± 0.05	Q 0833+446; RBS 711
13	08:42:15.30+40:25:33.3	2	S2	16.85	0.0553	2	8. ± 2.	15. ± 3.	1.05 ± 0.12	
14	08:46:22.54+03:13:22.2	3	S1.0	17.48	0.1070	−22	8.8 ± 0.5	7.9 ± 1.2	0.67 ± 0.06	
15	08:53:32.22+21:05:33.7	2	S2	17.73	0.0719	−32	6.2 ± 1.1	7. ± 2.	1.07 ± 0.11	
16	08:57:40.86+35:03:21.7	3	S1.5	19.25	0.2752	46	3.4 ± 1.6	10.8 ± 1.6	0.77 ± 0.08	
17	08:58:10.64+31:21:36.3	2	S2	18.23	0.1389	−15	6.1 ± 1.5	13.4 ± 1.7	1.03 ± 0.10	
18	09:17:15.00+28:08:28.2	3	S1.5	18.08	0.1045	−37	10.0 ± 1.2	19. ± 9.	0.35 ± 0.04	
19	09:18:25.79+00:50:58.4	3	S1.5	18.16	0.0871	−43	6.6 ± 0.7	11. ± 2.	0.79 ± 0.09	
20	09:23:43.00+22:54:32.6	3	NLS1	15.65	0.0330	51	8.2 ± 0.6	16.8 ± 0.9	0.37 ± 0.03	MCG +04-22-42
21	09:42:04.79+23:41:06.9	3	S1.5	15.92	0.0215	−49	7.0 ± 0.7	4.5 ± 1.8	1.19 ± 0.14	PGC 027720
22	10:01:49.52+28:47:09.0	2	S1.9	17.32	0.1849	17	6.3 ± 0.9	7. ± 2.	1.22 ± 0.08	3C 234
23	10:17:18.26+29:14:34.1	3	S1.5	16.71	0.0492	−66	3.8 ± 0.7	13. ± 2.	0.38 ± 0.05	
24	10:22:35.15+02:29:30.5	2	NLS1	18.71	0.0701	−84	8. ± 5.	8. ± 9.	0.76 ± 0.09	
25	10:34:38.60+39:38:28.3	2	NLS1	16.80	0.0435	−107	3.3 ± 0.4	6.6 ± 1.2	0.37 ± 0.02	KUG 1031+398
26	10:55:19.54+40:27:17.5	3	S1.5	17.49	0.1201	−27	2.3 ± 1.0	16. ± 2.	0.90 ± 0.09	Mrk 1269
27	11:02:43.20+38:51:52.6	2	NLS1	18.89	0.1186	−19	8.3 ± 1.3	18.8 ± 1.7	0.84 ± 0.09	1WGA J1102.7+3851
28	11:07:04.52+32:06:30.0	3	S1.5	17.64	0.2425	104	2. ± 3.	2.9 ± 1.3	1.25 ± 0.06	
29	11:07:16.49+13:18:29.5	3	S1.5	18.35	0.1848	−44	3.5 ± 0.7	10. ± 2.	0.56 ± 0.07	
30	11:07:56.55+47:44:34.8	3	S1.0	16.98	0.0727	3	5. ± 5.	16. ± 2.	0.40 ± 0.05	
31	11:09:29.10+28:41:29.2	2	S2	17.20	0.0329	−77	5. ± 3.	18. ± 11.	0.55 ± 0.05	
32	11:26:02.46+34:34:48.2	2	S1.9	17.92	0.1114	−78	1.9 ± 0.7	4.1 ± 1.9	1.18 ± 0.14	
33	11:31:07.10+11:58:59.3	3	S1.0	17.58	0.0910	2	4.3 ± 0.9	10. ± 3.	0.78 ± 0.09	
34	11:39:17.17+28:39:46.9	2	S2	17.05	0.0234	−11	9.5 ± 1.5	1. ± 4.	0.81 ± 0.09	
35	11:42:16.88+14:03:59.7	2	S2	16.44	0.0208	−48	6.4 ± 0.2	6.9 ± 0.5	0.95 ± 0.04	
36	11:52:26.30+15:17:27.6	3	S1.5	17.91	0.1126	2	2. ± 2.	12. ± 3.	1.15 ± 0.12	
37	11:57:04.84+52:49:03.7	2	S2	16.78	0.0356	−39	6.3 ± 0.8	12.1 ± 1.7	1.32 ± 0.10	
38	12:04:22.15–01:22:03.3	3	S1.0	17.58	0.0834	2	6. ± 4.	17. ± 9.	0.53 ± 0.07	
39	12:07:35.06–00:15:50.3	2	S2	18.84	0.1104	−28	2.6 ± 1.9	7. ± 4.	1.46 ± 0.17	
40	12:09:32.94+32:24:29.3	3	NLS1	17.94	0.1303	97	3.5 ± 0.8	11. ± 2.	1.32 ± 0.13	
41	12:10:44.28+38:20:10.3	3	S1.0	15.63	0.0230	−43	10.0 ± 1.4	15. ± 2.	0.82 ± 0.08	KUG 1208+386
42	12:29:03.50+29:46:46.1	2	S1.5	18.45	0.0821	−166	3.7 ± 1.3	6. ± 3.	1.02 ± 0.12	
43	12:29:30.41+38:46:20.7	2	S2	18.20	0.1024	−39	2.4 ± 0.6	0.5 ± 1.6	1.52 ± 0.16	
44	12:31:49.08+39:05:30.2	3	S1.5	17.50	0.0683	−39	6. ± 6.	5. ± 7.	0.86 ± 0.10	
45	12:41:34.25+44:26:39.2	2	gal	18.87	0.0419	18	10. ± 5.	1. ± 10.	0.33 ± 0.03	
46	13:11:35.66+14:24:47.2	3	NLS1	17.03	0.1140	−61	1.7 ± 0.8	17.8 ± 0.7	0.32 ± 0.03	
47	13:13:05.69–02:10:39.3	3	S1.0	16.70	0.0838	−20	3. ± 3.	17.5 ± 1.6	0.38 ± 0.04	
48	13:13:48.96+36:53:58.0	3	S1.5	17.59	0.0670	−66	6.4 ± 0.7	10. ± 2.	0.78 ± 0.08	
49	13:16:39.75+44:52:35.1	2	S2	17.37	0.0911	−55	2.9 ± 0.6	10.1 ± 1.9	1.03 ± 0.06	1WGA J1316.6+4452
50	13:19:57.07+52:35:33.8	2	NLS1	17.92	0.0922	−69	6.0 ± 0.8	15.4 ± 1.9	0.48 ± 0.03	RBS 1249
51	13:23:46.00+61:04:00.2	2	S2	17.58	0.0715	−36	2.5 ± 0.8	4.7 ± 1.0	2.37 ± 0.13	
52	13:46:07.71+33:22:10.8	3	S1.0	17.45	0.0838	−44	5. ± 5.	17. ± 4.	0.60 ± 0.07	
53	13:55:42.76+64:40:45.0	3	NLS1	16.73	0.0753	−42	3. ± 2.	15. ± 4.	0.48 ± 0.02	VII Zw 533
54	14:34:52.46+48:39:42.8	3	S1.0	15.93	0.0365	−8	6. ± 3.	17.3 ± 1.5	0.60 ± 0.06	NGC 5683; Mrk 474
55	15:32:22.32+23:33:25.0	2	S2	17.46	0.0465	−50	8. ± 2.	14. ± 2.	1.37 ± 0.14	
56	15:35:52.40+57:54:09.5	3	S1.0	15.21	0.0304	15	4.7 ± 1.0	17.1 ± 1.1	0.62 ± 0.06	Mrk 290
57	16:09:48.21+04:34:52.9	2	S2	17.77	0.0643	−91	6.7 ± 0.9	5. ± 2.	1.15 ± 0.07	
58	16:13:01.63+37:17:14.9	3	S1.0	16.46	0.0695	12	6.1 ± 1.6	16.0 ± 1.3	0.53 ± 0.05	KUG 1611+374B
59	16:18:44.85+25:39:07.7	3	NLS1	16.94	0.0479	9	8. ± 3.	18. ± 7.	0.36 ± 0.04	
60	16:35:01.46+30:54:12.1	3	S1.5	17.33	0.0543	−1	9.1 ± 1.6	16. ± 4.	0.43 ± 0.04	
61	20:58:22.14–06:50:04.4	3	NLS1	18.22	0.0740	−58	4.8 ± 0.7	8.1 ± 1.7	0.86 ± 0.10	
62	22:02:33.85–07:32:25.0	3	NLS1	17.05	0.0594	−6	4.0 ± 0.6	11.3 ± 1.6	0.76 ± 0.06	
63	22:15:42.30–00:36:09.8	3	S1.0	17.30	0.0994	−30	3.7 ± 1.0	11. ± 2.	0.98 ± 0.10	
64	23:56:54.30–10:16:05.5	3	S1.5	16.59	0.0740	−77	2.2 ± 0.3	14.6 ± 0.9	0.42 ± 0.02	

alternative common names. These represent a diverse range of Seyfert objects: 26 type 1s (including 12 NLS1s), 19 intermediate types (16 of type 1.5 and three of type 1.9) and 18 type 2 Seyferts (our working definitions for these spectral types are described in Section 3.2.5). In addition, we found one galaxy with an unusual spectrum that is not Seyfert like. It is listed in Table 1 (object 45, spectral type 'gal'), but is not included in the rest of this paper; it is discussed in detail in a separate study (Ward et al., in preparation). We note that 27 out of these 64 objects are spectroscopically classified by the SDSS pipeline as galaxies and not quasars: one non-Seyfert galaxy, all of the Sy2 and Sy1.9 sources, plus one Sy1.5 (Source 42) and four NLS1s (Sources 24, 25, 27 and 50).

This is one of the largest and by far the most homogeneous samples of AGN with strong FHILs to date. However, we note that this sample is by no means complete. There are certainly many other galaxies with strong [Fe X] emission in the SDSS catalogue that have been excluded by the [O I] significance or the Hα width criteria. Our selection criteria introduce biases against Sy1s with the broadest permitted lines and any FHIL-emitting sources dominated by lines with lower IPs (e.g. with low [Fe X]/[Fe VII] ratios). This is in addition to any biases inherited from the SDSS spectroscopic survey (e.g. the photometric criteria used by SDSS to select spectroscopic targets coupled with the fact that we directly observe the AGN continuum flux in Sy1s and not in Sy2s means that SDSS-selected type 1 objects will extend to higher redshifts and may include less intrinsically powerful nuclei). Nevertheless, the size and relative homogeneity of this sample make it useful for testing correlations between FHIL features and other properties.

3 ANALYSIS

In this paper, we focus our attention on the strongest FHILs and the most prominent other lines available for low-redshift objects within the SDSS spectral band. In the wavelength range $3500 < \lambda < 9000$ Å, the strongest observed lines with IPs $\gtrsim$100 eV are all species of iron: [Fe VII]λ6087, [Fe X]λ6374 and [Fe XI]λ7892. Other FHILs in this range include [Fe XIV]λ5303, [Fe XI]λ3987 and several [Fe VII] lines (notably ones at 5721, 5276, 5159, 4893, 3967 and 3586 Å; see e.g. Osterbrock 1981; Appenzeller & Öestreicher 1988; Erkens et al. 1997), but we do not measure these because they are not as strong, some are blended with other features and the shorter wavelength lines will be more strongly affected by any dust that is present. In addition to the three strongest iron FHILs, we also measure Hα and the following lower ionization forbidden lines: [O III]λ5007, [O I]$\lambda\lambda$6300, 6364, [N II]$\lambda\lambda$6548, 6583 and [S II]$\lambda\lambda$6718, 6730.

3.1 Spectral fitting procedure

We designed a set of IDL scripts to fit a series of models to the SDSS spectra. In order to minimize the complexity of these models, we made separate analyses of six bands around [O III], [Fe VII], [O I]+[Fe X], Hα+[N II], [S II] and [Fe XI]. In each interval, we first fit a low-order polynomial to establish the local continuum. This may include both true continuum and other broad components, notably the wings of any broad Hα components that sometimes extend to wavelengths near [Fe X] and [S II]. We therefore used a third-order polynomial in these two bands to allow for some curvature in the continuum model and a second-order polynomial in the other bands. This local continuum is subtracted from the data before applying a sequence of emission line models.

The sequence of models applied to each emission line starts with a single Gaussian. The initial fitting is done with the line profile parameters (width and centroid) fixed at assumed values in order to minimize the number of free parameters. Next, the profiles are allowed to vary (within limits: doublets are assumed to have the same profiles; additional constraints are described below) and the best-fitting parameters are determined. We then try adding a second Gaussian, using χ^2 statistics to test whether the added component provides a significantly better description of the data.[3] In the case of Hα, we also try adding a third Gaussian to the model, once again testing whether the added component is significant. The most detailed model that offers a significantly improved fit is adopted as the best-fitting model, provided that it passes a final visual inspection (described in the next section). The best-fitting models are presented online in Tables A1–A6. In Fig. 1, we demonstrate the best-fitting line models for one of our sample members in the [O III], [Fe VII], [Fe X](+[O I]) and Hα(+[N II]) bands (the [S II] and [Fe XI] line models are not shown because these are fitted with only a single Gaussian and are not blended).

Some notes on details of the line-fitting process are as follows.

(i) *Two-component forbidden line models:* the double-Gaussian model provides a significantly improved fit to the [O III] line for every member of our sample. The same cannot be said of the [Fe VII] line, which is found to require a second component in only 14 cases. The other forbidden line data generally do not require a second component so only single-Gaussian models are used. We note that the use of a mix of single- and double-Gaussian models to fit [Fe VII] does not introduce a strong systematic effect, as the fluxes of most compound models differ from those of best-fitting single Gaussians by no more than 15 per cent, which is comparable to the uncertainty in the measurements. The advantage of sometimes using the two-component model is a more accurate characterization of the profile of the *core* of the [Fe VII] lines.

(ii) *Blended lines:* in order to separate blended lines, additional constraints were applied. In the case of the [O I]+[Fe X], we first determined the best-fitting parameters for the [O I]λ6300 line. We then assumed an [O I]λ6364 model with the same width and velocity shift and one-third the intensity of [O I]λ6300 and fitted the [Fe X] model to the remaining flux. A similar process was used to deblend Hα and the [N II] doublet. If the [N II] models are not constrained, they will sometimes include a significant amount of Hα flux. This is especially problematic when the width of Hα is $\sim$1500 km s^{-1}, because the [N II] models can effectively slice off the broad-line wings, resulting in Hα models that are systematically too narrow. To mitigate this tendency, a Gaussian fitted to [O I]λ6300 was used as a template for the narrow-line emission profile. The [N II] models were assigned the same width and velocity shift as [O I], with only the intensity allowed to vary. These intensities were refitted with each successive Hα model.

(iii) Hα *model components:* up to three Gaussian components are used to model the Hα lines; the third is discarded as unnecessary in 21 instances. One of the Gaussians is forced to have the same width and velocity shift as the narrow-line template defined by [O I] (see previous comment on blended lines). Thus, the Hα model is guaranteed to have at least one component with the characteristics of the NLR.

[3] We consider a model to be significantly better if the probability of obtaining the same reduction in χ^2 by chance is <1 per cent.

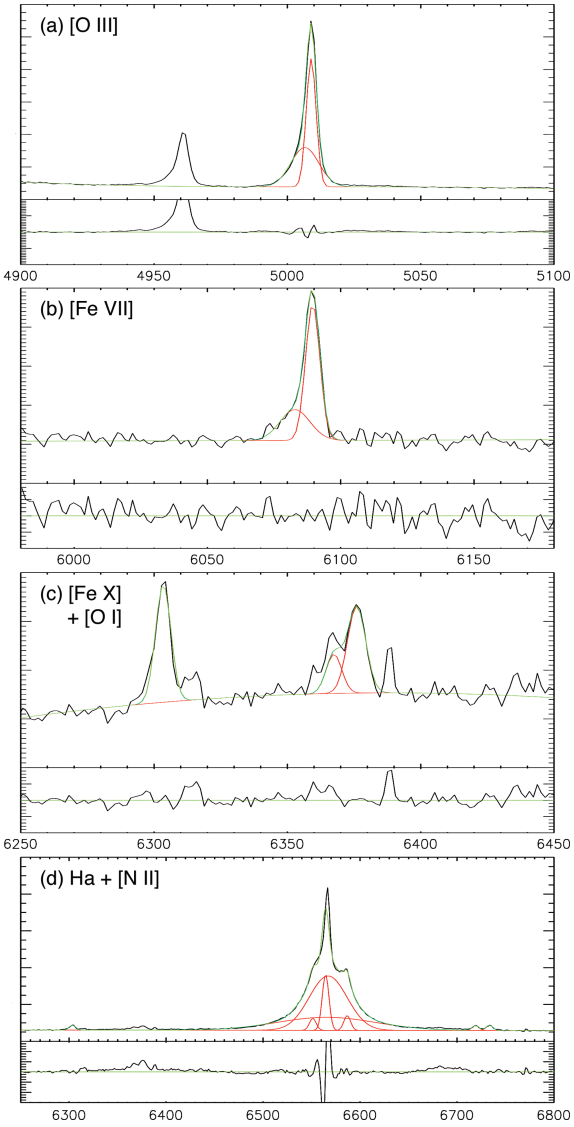

Figure 1. A demonstration of the multicomponent line models as applied to the NLS1 VII Zw 533 (Source 53). Pairs of panels show the data with the best-fitting models overlaid and the residuals after the models have been subtracted. From the top down are the [O III], [Fe VII], [Fe X] and Hα bands. Red curves are the individual model components; green curves are either the total model (in the data plots) or the zero line (in the residual plots). Note the distinct blue wing in both the [O III] and [Fe VII] line profiles. Wavelengths are in Å in the emitted frame (as defined by SDSS redshifts) and the flux density scale is arbitrary.

(iv) *[Fe XI] measurements:* SDSS does not provide spectral coverage at the wavelength of [Fe XI] for eight of our sample members (six are at $z > 0.16$; two others have gaps in their data). Of the remaining 55 AGN spectra, 36 provide [Fe XI] detections with >99 per cent confidence despite the increased noise due to OH sky lines at these wavelengths.

3.2 Optical parameter analysis

3.2.1 Rejection of spurious models

A final check of the best-fitting models was made to identify any dubious line model components. The most common mode of failure was when a second (or third) component of [Fe VII] or Hα became extremely broad to account for residual continuum flux. In such cases, we reverted to the best-fitting parameters of a previous, less complex model. Apart from these cases, there were four other best-fitting models that were revised after inspection. In two instances (Sources 40 and 48), [Fe XI] models were discarded because they were found to be fitted to sky line residuals. For Source 28, a Sy1.5 with a very broad Hα component, the [Fe X] Gaussian was used to model part of the continuum and had to be refitted manually. In one other object (Source 5, a Sy2 with relatively simple line profiles), one of the Hα components was fitted to [N II]λ6583; to correct this, its flux has been reassigned to the [N II] line.

3.2.2 Line velocity shifts and redshift redefinition

The velocity shifts ($v_{\rm sh}$) of the emission lines are measured relative to the recession velocities of their host galaxies. Hence, a negative velocity shift indicates a reduced recession velocity of a line-emitting region. We interpret $v_{\rm sh} < 0$ km s^{-1} as outflow velocities along our line of sight, although we cannot rule out the possibility of emission from infalling clouds approaching from the far side of the AGN.

In order to measure $v_{\rm sh}$ with the highest possible precision, care must be taken in how the systemic redshifts are defined. The SDSS pipeline uses multiple methods to measure redshifts; the final value is defined by the method that yields the highest confidence measurement. However, there can be systematic differences between the redshift values determined by these methods (e.g. when emission lines are dominated by outflows and are used as the basis of the redshift measurement). Such systematics may be present at the few hundred km s^{-1} level even when the SDSS pipeline reports that the measurements are mutually consistent (as is the case for 46 out of 63 sample members). Therefore, if we are to measure $v_{\rm sh}$ with precision better than a few hundred km s^{-1} and avoid systematic effects, we must ensure that a consistent definition of redshift is used for our entire sample.

Ideally we would define systemic redshifts from the stellar properties of the host galaxies, but not all of our sample members have measurable absorption features. Instead, we base our definition upon the centroid wavelengths of the [S II] doublet. This doublet is chosen because it has a low IP and a low critical density ($N_{\rm cr}$). Therefore, amongst the emission lines available in all our spectra, this is the feature most likely to be dominated by regions farthest from the central engine, where the influence of the AGN is expected to be weakest. Thus, the [S II] lines should be more closely related than any other available feature to the kinematics of the ISM of the host galaxy. However, it is possible that these lines may sometimes arise in outflowing gas. In such cases, the line centroid will not accurately indicate the systemic velocity of the host if the observed velocity structure is not symmetric (e.g. if there is a biconal outflow and we do not integrate comparable amounts of flux from both sides).

The change from SDSS-defined to [S II]-defined redshifts results in a range of $v_{\rm sh}$ adjustments from -166 to $+103$ km s^{-1}. The median adjustment is -34 km s^{-1}, so the redshift redefinition tends to increase the outflow velocities. All $v_{\rm sh}$ values reported in this paper are measured relative to the [S II]-defined redshifts. It is worth noting that the $v_{\rm sh}$ values of [O I] and the *core* of [O III] (defined in the next section) agree very well with those of [S II], with mean values of 0 ± 4 and -5 ± 5 km s^{-1}, respectively. This agreement is somewhat surprising because the critical densities of these lines are larger by factors of 10^3 and $10^{2.5}$, so their emission is expected to be dominated by different regions.

3.2.3 *[O III] and [Fe VII] components*

For every source in this sample, the two-component line model provided a significantly better fit to the [O III] profile than did the single-Gaussian model. In most cases, the second component was used to represent asymmetric line profiles. We therefore adopt the nomenclature of 'core' and 'wing' components of the line ($[O\,III]_C$ and $[O\,III]_W$, respectively), with the core defined to be the component whose centre is closer to the peak of the overall profile. The core is invariably the Gaussian with the smaller FWHM. With this definition, 53 [O III] lines have blue wings, six have red wings and five have components separated by less than 1/4 pixel (<17 km s^{-1}; see Table A4).

Unlike [O III], double-Gaussian models seldom provide a significantly better fit to the [Fe VII] lines. When two Gaussians are used, we again divide them into core and wing components ($[Fe\,VII]_C$ and $[Fe\,VII]_W$). In all cases, we find that $[Fe\,VII]_W$ is both broader and bluer than $[Fe\,VII]_C$. In the remaining 49 cases, the single-Gaussian model is used as $[Fe\,VII]_C$ (hence $[Fe\,VII]_{1G} = [Fe\,VII]_C$ for most sample members). The best-fitting [Fe VII] models are presented in Table A3. This table includes the best-fitting single-Gaussian models for all sample members, even those for which the double-Gaussian model provides a significant improvement, in order to provide a model that is uniform across the entire sample. We use the notation $[Fe\,VII]_{1G}$ when we refer to the single-Gaussian models for the entire sample.

We note that there is a potential degeneracy when deblending the core and wing line components. If too much or too little flux is attributed to the core, then the width and velocity shift of the wing can be affected. At best, this degeneracy introduces an additional uncertainty in the parameters of the individual components, contributing noise to the data; at worst, it can introduce systematic effects that skew the average values across the sample. Thus, the core and wing components may be thought of as a possibly non-physical parametrization of an asymmetric line profile. As such, the properties of these individual components, especially those of the wing, may best be interpreted qualitatively. Although the exact details of these components may be suspect, they do provide a more accurate description of the shape of the line profile than a single-Gaussian model could. Moreover, the flux of the combined model provides a better measure of the actual flux from the line. We therefore consider the sum of the component fluxes to be a robust measure of the line strength, and will emphasize this in the ensuing discussion. Hereafter, we use the subscript 'T' when referring to this combined flux.

3.2.4 Hα *components*

The Hα lines are fitted with up to three Gaussian components. These models generally have one narrow, one intermediate and one broad component (a third component is rejected in only 21 instances). However, sometimes more than one of these had a full width at half-maximum (FWHM) comparable to that of [O I]. Clearly, the intermediate-width component did not consistently represent a distinct region: sometimes it was unambiguously broad (FWHM $>$ 2000 km s^{-1}), other times it was used to fine-tune the modelling of the NLR contribution to Hα. We therefore decided to combine the Gaussians into two Hα components: $H\alpha_N$, interpreted as the NLR contribution to Hα, combines all components not much broader than [O I] and $H\alpha_B$, the BLR contribution, includes all Gaussians substantially broader than [O I]. The ratios of Hα component FWHM over [O I] FWHM almost always had values $\leq$1.3 or $\geq$2.8 (Fig. 2),

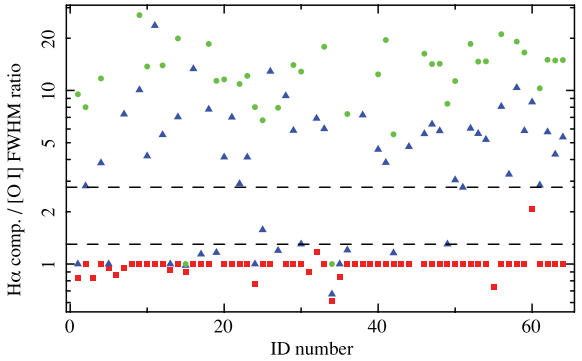

Figure 2. Ratios of the Hα component widths over [O I] FWHM. Red squares, blue triangles and green circles represent the FWHM ratios of progressively broader Hα Gaussian components over [O I] λ6300. Dashed lines are drawn at ratios of 1.3 and 2.8. Components that fall below the lower line are assigned to $H\alpha_N$ whilst those above the higher line are assigned to $H\alpha_B$; the few points between are considered individually. By construction, all Hα models include one Gaussian with the FWHM of [O I] unless this component is found to be insignificant.

so these thresholds were used to define $H\alpha_N$ and $H\alpha_B$ components.[4] When $H\alpha_N$ or $H\alpha_B$ consists of more than one component, the flux used is the sum of the components and the profile is that of the highest flux Gaussian. As with $[O\,III]_T$ and $[Fe\,VII]_T$, we use $H\alpha_T$ when referring to the combined flux of all the Hα components.

3.2.5 *Spectroscopic classifications*

The first challenge in establishing the spectroscopic classifications of our sample members is to separate the Sy2s from the other Seyfert types. Simply using the FWHM of the broadest Hα component is problematic because in several Sy2s (the ones with strong [O III] wings), the Hα models include a weak but statistically significant broad component. This component appears to be real but its width (FWHM sometimes 2000 km s^{-1} or more; cf. Table A6) is non-physical, in that it is fitted to the blended, otherwise-unmodelled blue wings of Hα +[N II] emission from the NLR. Another complication is that the $H\alpha_B$ FWHM of the narrowest NLS1s is comparable to the broadest $H\alpha_N$ lines amongst the Sy2s. Instead of using Hα FWHM, we use two line flux ratios, $[N\,II]/H\alpha_T$ and $[O\,III]_T/H\alpha_T$. The total Hα flux is a strong discriminator between Sy2 and other Seyfert types because lines that include a broad component usually have much more flux, but neither ratio alone is sufficient as a single parameter to separate the Sy2s because there is some overlap with other Seyfert types. However, following the approach of Baldwin, Phillips & Terlevich (1981), we find that the Sy2s are very well separated from all other AGN in the plane defined by these two ratios (Fig. 3; see also Zhang et al. 2008). All of the Sy2s in the present study are bounded by $\log([O\,III]_T/H\alpha_T) > 0$ and $\log([N\,II]/H\alpha_T) > -0.5$. These ratios have not been corrected

[4] Just two best-fitting Hα models had components with velocity widths between these limits and therefore required special consideration. The intermediate-width Hα component of the NLS1 galaxy KUG 1031+398 (Source 25) has FWHM = 1.6 × FWHM [O I]; this is considered part of $H\alpha_B$. The narrowest Hα component fitted to the Sy1.5 IRAS F16330+3100 (Source 60) has FWHM = 2.1 × FWHM [O I], but this is a reasonable fit to what is clearly a narrow component of Hα with a double peak, so it is assigned to $H\alpha_N$.

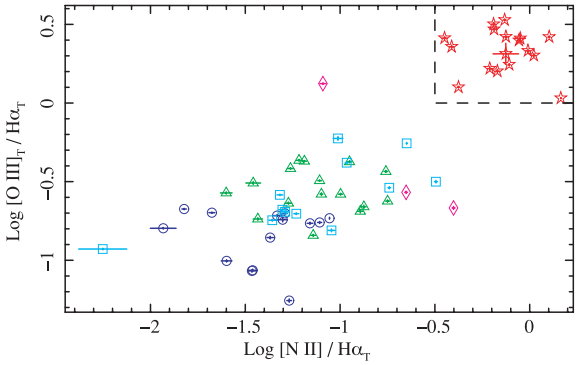

Figure 3. Line diagnostic ratios used to separate Sy2s from other Seyferts. Sy2s (red stars) are bounded by $\log([\mathrm{O\,III}]_T/\mathrm{H}\alpha_T) > 0$ and $\log([\mathrm{N\,II}]/\mathrm{H}\alpha_T) > -0.5$. The other sample members are classified as Sy1.9s (magenta diamonds), Sy1.5s (green triangles), NLS1s (cyan squares) and Sy1.0s (blue circles) according to their H line profiles.

for reddening, which would tend to increase the $[\mathrm{O\,III}]_T/\mathrm{H}\alpha_T$ values. However, Sy2s generally require the largest corrections, so accounting for reddening would strengthen their separation in this plane.

Once the Sy2s are separated, the remaining type 1 AGN are classified based on the properties of their Balmer lines. The 12 sources with $\mathrm{H}\alpha_\mathrm{B}$ FWHM < 2200 km s^{-1} are defined to be NLS1; the other type 1 Seyferts collectively comprise the broad-lined Seyferts (BLS1). Note that the division between NLS1s and BLS1s is somewhat arbitrary,[5] but we apply it here to compare with previous work and to see if other properties distinguish this subclass. The BLS1s are subdivided into three groups: the ones with very little $\mathrm{H}\alpha_\mathrm{N}$ emission are Sy1.0s (based upon the fraction of the overall Hα flux in the $\mathrm{H}\alpha_\mathrm{N}$ component, with a subjectively chosen threshold of no more than 8 per cent); most of the rest, with larger $\mathrm{H}\alpha_\mathrm{N}/\mathrm{H}\alpha_\mathrm{B}$ ratios, are Sy1.5s; the few with no clear broad component at Hβ are classified as Sy1.9s. The final tally of spectral types is 14 Sy1.0s, 12 NLS1s, 16 Sy1.5s, three Sy1.9s and 18 Sy2s.

3.2.6 *Estimates of dust reddening*

The measured line fluxes are not corrected for reddening. The impact of dust is generally small, as most sample members appear to have very little reddening (based upon both the Balmer decrements and the shapes of the continua). Furthermore, it is difficult to measure the Balmer decrement reliably for many type 1 Seyferts because of the difficulty in separating $\mathrm{H}\alpha_\mathrm{N}$ from $\mathrm{H}\alpha_\mathrm{B}$, rendering any correction uncertain. Amongst the few spectra that do appear to be affected by dust, the most reddened objects are Sources 7, 13 and 32; two Sy2s and a Sy1.9 for which we estimate $A_V = 3.3$, 3.5 and 2.9, respectively. In no other Seyfert have we found $A_V > 2.2$. To mitigate the effect of any uncorrected reddening, we will place some emphasis on comparisons of lines that are close in wavelength. For instance, with $A_V < 2.2$ for the rest of the sample, the effect upon [Fe VII]/[Fe X] ratios will be $\leq$10 per cent and is always smaller than the measurement uncertainty.

[5] The specific FWHM threshold adopted to define NLS1s is the same as that used by Zhou et al. (2006), but is a bit broader than the more commonly used value of 2000 km s^{-1} (e.g. Goodrich 1989). Our choice is motivated by the data, in that there is a break in the distribution of $\mathrm{H}\alpha_\mathrm{B}$ FWHM values around 2200 km s^{-1}.

Table 2. Final spectral line models used for analysis.

Emission line	IP (eV)	log N_{cr} (cm^{-3})	Comp. count	Details of final fit
[O III]λ5007	35.1	5.8	2	Core and wing components
[Fe VII]λ6087	99.1	7.6	1–2	Only 14 final models include wing component
[O I]λ6300	–	6.3	1	All parameters free
[O I]λ6364	–	6.3	1	Parameters defined by [O I]λ6300
[Fe X]λ6374	233.6	9.7	1	All parameters free
[N II]λ6548	14.5	4.9	1	[N II] v_{sh} and FWHM
[N II]λ6584	14.5	4.9		defined by [O I]λ6300
Hα	–	–	2	Broad and narrow comps.
[S II]λ6716	10.4	3.2	1	[S II] doublet fitted with
[S II]λ6731	10.4	3.6		single v_{sh} and FWHM
[Fe XI]λ7892	262.1	10.4	1	36 [Fe XI] det., 19 non-det.

Note. [O I]λ6300 is used as a template for the parameters of the [O I]λ6364 model in order to deblend [O I]+[Fe X], and for the profile of the NLR when fitting Hα+[N II]. Columns are (1) line ID; (2) IP (eV); (3) log of the critical density at $T = 10^4$ K for the forbidden transition lines (cm^{-3}); (4) number of model components used and (5) details regarding parameter constraints and (in the cases of [Fe VII] and [Fe XI]) the frequency with which models are considered significant.

3.2.7 *Summary of the final line profile models*

The final set of models adopted for the discussion that follows is summarized in Table 2. The [O III] and [Fe VII] lines fitted with two Gaussians are organized into core and wing components, as described in Section 3.2.3. The Hα lines are fitted with up to three Gaussians which are then combined into two components, 'broad' and 'narrow' ($\mathrm{H}\alpha_\mathrm{B}$ and $\mathrm{H}\alpha_\mathrm{N}$; Section 3.2.4). For these lines, which at least sometimes include more than one component, we use the subscript 'T' (i.e. $[\mathrm{O\,III}]_T$, $[\mathrm{Fe\,VII}]_T$ and $\mathrm{H}\alpha_T$) to refer to the combined fluxes of all components. The remaining lines (the [O I], [N II] and [S II] doublets, [Fe X] and [Fe XI]) are fitted with single-Gaussian models. For many of the NLR lines, the model parameters are linked to each other. In particular, the [O I]λ6364 model is completely defined by the fit to [O I]λ6300. Because of this, unless 6364 Å is specified, any mention of [O I] will implicitly refer to the stronger line at 6300 Å.

3.3 *ROSAT* X-ray data

Half of our sample members (32 out of 63) appear in catalogues of soft X-ray sources detected with the *ROSAT* Position Sensitive Proportional Counter (PSPC).[6] We convert the PSPC count rates to fluxes using the PIMMS tool from High Energy Astrophysics Science Archive Research Center (HEASARC),[7] assuming a power-law model with a photon index $\Gamma = 1.5$ and an intervening absorption column of $n_\mathrm{H} = 3 \times 10^{20}$ cm^{-2} at $z = 0$. It is well established that NLS1s often have much steeper soft X-ray spectral indices than other Seyfert galaxies (Boller 2000), so we also consider the effect of using $\Gamma = 3.0$ for the NLS1s. Given these assumed models, the conversion from RASS count rates to fluxes in the full 0.1–2.4 keV *ROSAT* band is equivalent to multiplicative factors of 1.30×10^{-11} and 8.12×10^{-12} erg cm^{-2} count^{-1} for $\Gamma = 1.5$ and 3.0,

[6] 28 were detected in the RASS (Voges et al. 1999, 2000). Four others appear in the White, Giommi & Angelini (2000) catalogue of sources found in pointed *ROSAT* observations.

[7] Online at http://heasarc.gsfc.nasa.gov/Tools/w3pimms.html

respectively. In Section 5.2, we make use of the estimated flux of these two models in a narrow band starting at the IP of [Fe X] (233–300 eV). The fractions of the overall *ROSAT* flux that lies in this soft X-ray band are 0.0216 if $\Gamma = 1.5$ and 0.108 if $\Gamma = 3.0$. Thus, the count rate conversion factors for this soft-band flux are 2.81×10^{-13} and 8.75×10^{-13} erg cm^{-2} count^{-1} (the *ROSAT* PSPC count rates, RASS hardness ratios and estimated fluxes are provided online in Table A7).

4 RESULTS

4.1 Sample statistics

The final sample consists of 63 Seyfert galaxies, all with measured [Fe X], [Fe VII] and [O III] fluxes. Included amongst these are 36 sources with measured [Fe XI], twice as many as any previous study. The only earlier sample that has a comparable number of AGN with FHIL measurements is that of NTM00. We will therefore use their sample for comparison in this and the following section. We note that NTM00 have 65 sample members with measured ratios of both [Fe X]/[O III] and [Fe VII]/[O III]; of these, only 47 have reported [O III] fluxes and 17 have [Fe XI] detections.

We have cross-correlated the SDSS [Fe X] sample with X-ray and radio catalogues. As noted in Section 3.3, 32 sample members have been detected by *ROSAT*. These include 11 out of 14 Sy1.0s, 10/12 NLS1s, 8/16 Sy1.5s, 0/3 Sy1.9s and 3/18 Sy2s. To determine which of the [Fe X] sources are radio loud, we obtained fluxes or flux limits from the FIRST (Becker, White & Helfand 1995) and NVSS (Condon et al. 1998) surveys. These are combined with the rest-frame flux density at 4400 Å (including an estimated reddening correction) to define the radio-to-optical flux density ratio R. Only one sample member is unambiguously radio loud (Source 22, 3C 234, with $R \sim 1.7 \times 10^4$). Several others are borderline radio-loud objects, with R values around 10, the strongest of which are Sources 25 ($R = 17$), 6 ($R = 10$) and 51 ($R = 8$).

We present the redshift distribution of the SDSS [Fe X] sample in Fig. 4 (top panel). There are no significant differences between the distributions of the Sy1.0, 1.5 and 1.9 populations, so these are combined as the BLS1 distribution. The principle difference between the Seyfert types is that only BLS1s are found beyond $z > 0.14$. Amongst the $z < 0.14$ sources, the median redshifts of the BLS1s, NLS1s and Sy2s are 0.082, 0.072 and 0.068, respectively. The Sy2s are the most locally concentrated group, revealing a selection bias against these sources. The greater incompleteness of type 2 Seyferts at even modest redshifts is suggestive of a flux limit affecting our source selection. This is likely a bias inherited from the SDSS. Sy2s both lack a strong AGN contribution to their optical continuum and are more likely to be reddened, so their photometric magnitudes are more likely to fall below the $r = 17.77$ mag completeness limit of the SDSS spectroscopic survey. Indeed, most (five out of six) Sy2s in our sample with $0.09 < z < 0.14$ have magnitudes within a few tenths of this limit, whereas only one-third (four out of 12) Sy1.0 and Sy1.5s in the redshift range $0.09 < z \leq 0.18$ appear this faint. However, it is also possible that Sy2s are weaker sources of [Fe X] emission, which would contribute to the dearth of these objects at higher redshifts.

The [Fe X]-selected sample redshift distributions may be compared to more broadly defined samples of SDSS sources. The distribution of BLS1s, and of the overall sample, is consistent with the distribution of all galaxies and quasars in the SDSS DR6 with $z < 0.28$ (grey histogram, Fig. 4, middle panel). We note, however, that the set of all 1098 quasar and galaxy spectra that satisfy our redshift, Hα and [O I] emission line criteria (with or without evidence of [Fe X] emission; i.e. criteria i–iv in Section 2) is more strongly skewed towards low redshifts (black outline histogram, Fig. 4, middle panel). Thus, the [O I]-emitting galaxies must consist of two populations: one in which [Fe X] is not detected that is very local and the [Fe X]-selected sample that more closely follows the redshift distribution of the overall SDSS parent population. Lastly, we note that the [Fe X]- and [Fe VII]-detected portion of the NTM00 sample (Fig. 4, bottom panel) is much more locally concentrated than any of the other samples.

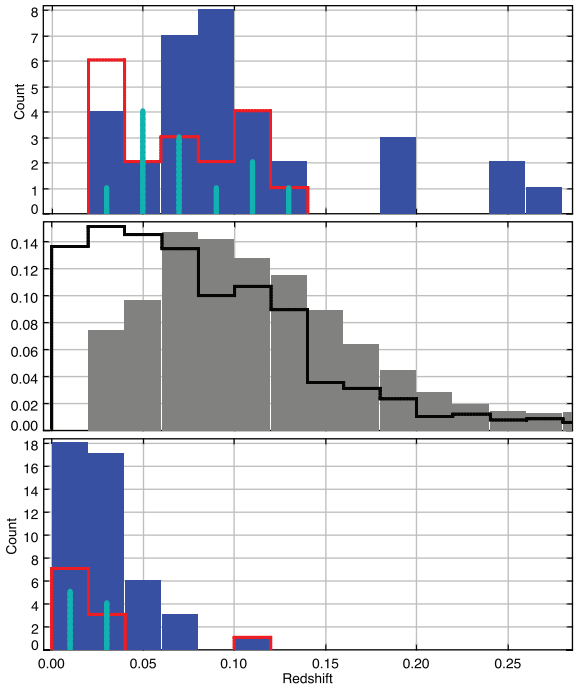

Figure 4. Redshift distributions. The [Fe X]-selected sample (top panel) is subdivided by spectral type: broad blue bars represent BLS1s including all intermediate types (Sy1.0–1.9), narrow light blue spikes depict the NLS1s and red outlines indicate the distribution of Sy2s. For comparison, we present broader samples drawn from the SDSS DR6 (middle panel): all ∼600 000 galaxies and quasars with $z < 0.28$, and the 1098 [O I]-emitting sources that satisfy criteria (i) through (iv) of Section 2 (grey filled-in histogram and black outline, respectively, with a normalized scale). The 65 NTM00 sources with reported [Fe X]/[O III] and [Fe VII]/[O III] ratios (bottom panel) are subdivided between BLS1s, NLS1s and Sy2s with the same symbols as the [Fe X] sample.

4.2 Line strengths

The distribution of [O III]$_T$ luminosities ($L_{[\mathrm{O\,III}]_T}$) is similar amongst the BLS1s, NLS1s and Sy2s in the [Fe X]-selected SDSS sample (Fig. 5, top panel). The only clear difference is that the BLS1s extend to higher $L_{[\mathrm{O\,III}]_T}$; these correspond to the highest redshift members of the sample. The distributions of NTM00 are comparable except that a few of their lowest redshift objects are found at considerably lower $L_{[\mathrm{O\,III}]}$ values (Fig. 5, bottom panel). Thus, apart from a few sources at the extremes of the redshift distributions, the [O III] power is reasonably well matched between the SDSS sample members of different spectral types and between the SDSS and NTM00 samples.

In Table 3, we present the correlation statistics between the fluxes of selected lines, line components and the X-ray band (scatter plots demonstrating many of these correlations are provided online in

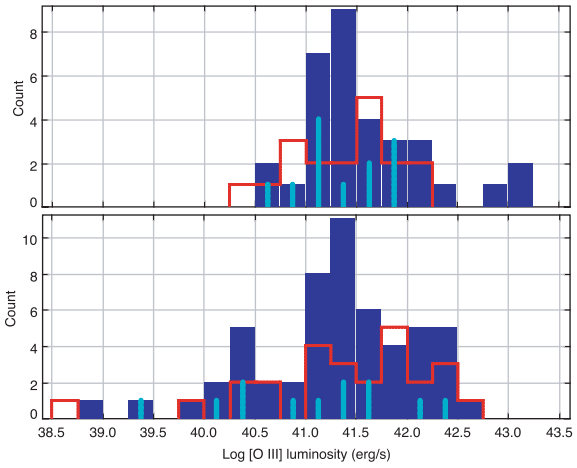

Figure 5. Distributions of [O III] luminosities amongst BLS1s NLS1s and Sy2s (symbols as in Fig. 4, top panel). The upper panel includes $[O\,III]_T$ luminosities for the 63 SDSS sample members; the lower panel presents the distributions for the 92 NTM00 objects with reported [O III] luminosities. These luminosities have been re-evaluated using *WMAP* cosmological parameters.

Figs A1–A5). We find that all fluxes are positively correlated. This is to be expected because, in general, the more powerful AGN should be stronger emitters of both X-ray continuum and various lines. The more interesting questions to ask are which parameters correlate most strongly, with the least scatter, and whether any trends are present when ratios are used to normalize fluxes. These are summarized in Table 4, in which the average flux ratios and the rms about each average are presented for the same pairs of fluxes appearing in Table 3.

Not unexpectedly, one of the best correlations, in terms of both strength (as measured by the Spearman rank correlation coefficient, ρ) and scatter (rms about the mean ratio), is between [Fe X] and [Fe XI] (Fig. 6). The mean [Fe XI]/[Fe X] ratio is 0.95 ± 0.08[8] for the 36 sources in which we detect [Fe XI]. Henceforth, we focus upon [Fe X] and not [Fe XI] when discussing the flux of the highest ionization lines, as this line provides higher S/N, offers more detections and is closer in wavelength to the other measured lines.

Apart from [Fe XI], the flux that correlates most strongly with [Fe X] is $[Fe\,VII]_T$. The correlations with $[O\,III]_T$, $[O\,III]_C$, $H\alpha_N$ and X-ray fluxes are comparable to each other and not much weaker than that with $[Fe\,VII]_T$.

The next highest ionization species in this study is [Fe VII]. Its IP is mid-way between those of [Fe X] and [O III] (2.4× lower than the former and 2.8× higher than the latter), so it is unclear a priori whether [Fe VII] will have properties more like the higher IP FHILs or the traditional NLR. As noted above, the flux of $[Fe\,VII]_T$ correlates well with [Fe X]. However, the strongest correlation and the smallest rms scatter amongst the $[Fe\,VII]_T$ flux ratios are provided by $[O\,III]_T$. We note that of the two [O III] components, the flux of $[O\,III]_W$ is more closely correlated with $[Fe\,VII]_T$, with $\rho = 0.762$ and rms = 0.29.

[8] Here, we have not accounted for the effect of dust, which is generally small (Section 3.2.6). When we apply estimated reddening corrections based upon the observed Balmer decrements, we obtain a mean [Fe XI]/[Fe X] ratio of 0.81 ± 0.07.

It is worth noting that when we use $[O\,III]_T$ strength to normalize $[Fe\,VII]_T$, we do not find any significant differences between the NLS1, BLS1 and Sy2 populations (Fig. 7, top panel). This contradicts MT98 and NTM00, who find that Sy2s have substantially lower [Fe VII]/[O III] ratios (Fig. 7, bottom panel). In addition, NTM00 report a similar, albeit weaker, disparity in the distributions of [Fe X]/[O III] ratios between types 1 and 2 Seyferts. Our [Fe X] data show something qualitatively similar, in that the [Fe X]/[O III] ratios of Sy2s tend to be lower than those of Sy1s, but quantitatively the difference we find is neither as large nor as significant as that reported by NTM00.[9] These conflicting results are likely a consequence of how the samples are selected. The earlier studies used heterogeneous collections of nearby, well-known Seyferts with data drawn from the literature. In particular, 31 out of 65 sources for which NTM00 report both [Fe X]/[O III] and [Fe VII]/[O III] ratios have lower redshifts than any member of the SDSS [Fe X] sample (Fig. 4, bottom panel). This contrast is most pronounced for the obscured Seyferts: 18 out of 28 Sy1.9 and Sy2s are closer than any of the SDSS sources. As a result of this proximity and consequently the larger angular scale of the galactic structures, the observers may have been better able to isolate the unresolved nuclear emission from the extended flux. Thus the contamination due to stellar light may be reduced, allowing for the discovery of weaker nuclear features in a subset of their sample. Additionally, the area integrated might not have covered the full extent of the NLR, thereby affecting the observed flux ratios in some systems. The [Fe X]-selected sample is more homogeneous, but our selection by [Fe X] creates a bias favouring sources with generally strong FHIL emission, reducing our sensitivity to low $[Fe\,VII]_T$/[O III] ratios as well as [Fe X]-weak spectra. Moreover, we note that 38 per cent of the [Fe VII]-detected sources in the NTM00 sample do not have [Fe X] detections. It is possible that there is a significant population of [Fe X]-weak Seyferts that are missing from the present sample.

For the overall sample, the next best $[Fe\,VII]_T$ correlation after [O III] is with [Fe X] (Fig. 8). However, we find that there is a systematic offset in this plane between the NLS1s and the Sy2s. Comparing linear regressions fitted to these two subsamples, we find that the [Fe X]/$[Fe\,VII]_T$ ratios of NLS1s tend to be two to three times higher. Whilst the line fitted to the NLS1s is influenced by a few notable outliers and there is some overlap between these subsamples, not one NLS1 lies below the line fitted to the Sy2s (red dashed line). Table 3 shows that $[Fe\,VII]_T$ also correlates very well with $H\alpha_T$, but this is only true when Sy2s are excluded from the analysis ($H\alpha_T$ is dominated by $H\alpha_B$ in the type 1 Seyferts, whereas by definition the $H\alpha$ lines in Sy2s do not have any BLR contribution; Fig. A3c). The weakest [Fe VII] correlation and the worst scatter are provided by X-ray flux (Fig. A5d), in contrast to the case of [Fe X] and X-rays.

The most prominent of the lower ionization forbidden lines is [O III]. The $[O\,III]_T$ flux correlates well with all of the other lines with IP < 100 eV ($\rho \geq 0.75$). However, it is [O I] that correlates best when all spectral types are considered, followed by $[Fe\,VII]_T$. When we consider only the type 1 Seyferts, we find that $[O\,III]_T$ correlates comparably well with $H\alpha_T$ as with [O I] and $[Fe\,VII]_T$ ($\rho = 0.82$, 0.82 and 0.80, respectively).

[9] The peaks in our types 1 and 2 Seyfert [Fe X]/[O III] distributions are separated by only 0.2–0.4 dex, whereas NTM00 show a separation of 0.6–0.8 dex. For our sample, the separation is not significant: a Kolmogorov-Smirnov (KS) test indicates a >10 per cent chance that these [Fe X]/[O III] ratios are drawn from the same parent population.

Table 3. Correlation statistics amongst selected line and X-ray fluxes.

	[O I]	Hα_N	Hα_T[a]	[O III]$_T$	[Fe VII]$_T$	[Fe X]	[Fe XI][b]	F_x[c]
[O I]	–	0.760 (−12.2)	0.760 (−8.9)	0.856 (−18.4)	0.739 (−11.3)	0.650 (−8.1)	0.590 (−3.8)	0.603 (−3.3)
Hα_N	0.760 (−12.2)	–	0.559 (−4.2)	0.752 (−11.9)	0.628 (−7.4)	0.659 (−8.4)	0.666 (−5.0)	0.539 (−2.6)
Hα_T[a]	0.760 (−8.9)	0.559 (−4.2)	–	0.824 (−11.5)	0.748 (−8.4)	0.590 (−4.7)	0.640 (−3.0)	0.514 (−2.4)
[O III]$_T$	0.856 (−18.4)	0.752 (−11.9)	0.824 (−11.5)	–	0.820 (−15.7)	0.647 (−8.0)	0.587 (−3.8)	0.465 (−2.0)
[Fe VII]$_T$	0.739 (−11.3)	0.628 (−7.4)	0.748 (−8.4)	0.820 (−15.7)	–	0.704 (−9.9)	0.617 (−4.2)	0.383 (−1.4)
[Fe X]	0.650 (−8.1)	0.659 (−8.4)	0.590 (−4.7)	0.647 (−8.0)	0.704 (−9.9)	–	0.884 (−12.0)	0.646 (−3.8)
[Fe XI][b]	0.590 (−3.8)	0.666 (−5.0)	0.640 (−3.0)	0.587 (−3.8)	0.617 (−4.2)	0.884 (−12.0)	–	0.600 (−1.6)
F_x[c]	0.603 (−3.3)	0.539 (−2.6)	0.514 (−2.4)	0.465 (−2.0)	0.383 (−1.4)	0.646 (−3.8)	0.600 (−1.6)	–

[a]Hα_T correlations include only the 45 type 1 Seyferts, as the Sy2s have only Hα_N components.
[b]Only the 36 detections are used to evaluate most [Fe XI] correlations; 23 type 1 Seyferts are used for Hα_T–[Fe XI], 14 for F_x–[Fe XI].
[c]F_x (0.1–2.4 keV) correlation statistics are based upon the 29 type 1 Seyferts with *ROSAT* detections (14 sources in the case of [Fe XI]).
Spearman rank correlation coefficient, ρ, and the log of the null hypothesis probability (i.e. the probability of finding by chance a correlation this strong between two parameters that are intrinsically not correlated; in parentheses) for selected emission line and X-ray fluxes. Probabilities are based upon the full sample of 63 objects unless noted otherwise. Values are repeated in the upper-right and lower-left halves of the table for convenience.

Table 4. Log of the average flux ratios, with rms.

	[O I]	Hα_N	Hα_T[a]	[O III]$_T$	[Fe VII]$_T$	[Fe X]	[Fe XI][a]	F_x[a]
[O I]	–	1.00 (0.24)	2.01 (0.26)	1.38 (0.18)	−0.02 (0.30)	−0.25 (0.29)	−0.18 (0.34)	3.28 (0.41)
Hα_N	−1.00 (0.24)	–	1.00 (0.36)	0.37 (0.24)	−1.02 (0.36)	−1.26 (0.31)	−1.19 (0.34)	2.33 (0.45)
Hα_T[a]	−2.01 (0.26)	−1.00 (0.36)	–	−0.64 (0.24)	−2.07 (0.29)	−2.22 (0.37)	−2.08 (0.42)	1.22 (0.48)
[O III]$_T$	−1.38 (0.18)	−0.37 (0.24)	0.64 (0.24)	–	−1.40 (0.27)	−1.63 (0.31)	−1.54 (0.36)	1.91 (0.45)
[Fe VII]$_T$	0.02 (0.30)	1.02 (0.36)	2.07 (0.29)	1.40 (0.27)	–	−0.23 (0.33)	−0.23 (0.37)	3.37 (0.51)
[Fe X]	0.25 (0.29)	1.26 (0.31)	2.22 (0.37)	1.63 (0.31)	0.23 (0.33)	–	−0.02 (0.18)	3.52 (0.38)
[Fe XI][a]	0.18 (0.34)	1.19 (0.34)	2.08 (0.42)	1.54 (0.36)	0.23 (0.37)	0.02 (0.18)	–	3.43 (0.55)
F_x[a]	−3.28 (0.41)	−2.33 (0.45)	−1.22 (0.48)	−1.91 (0.45)	−3.37 (0.51)	−3.52 (0.38)	−3.43 (0.55)	–

[a]As noted in Table 3, these ratios are based upon subsets of the [Fe X] sample: 45 type 1 Seyferts for ratios involving Hα_T, the 29 type 1 Seyferts with X-ray detections for ratios involving F_x and the 36 [Fe XI]-detected sample members (of any spectral type) for the [Fe XI] ratios.
Log of the average flux ratios with rms scatter about each mean (within parentheses, reported in dex). Fluxes in the numerator are given across the top and those in the denominator are listed at the left. Thus, the entries in the first row are log(Hα_N/[O I]), log(Hα_T/[O I]), log([O III]$_T$/[O I]), etc. Formal statistical uncertainties for the average ratios are ±0.03–0.05 for ratios defined by the full [Fe X] sample and can be as large as ±0.10 for ratios involving [Fe XI], Hα_T or F_x due to the smaller subsamples upon which these are based (in the case of the [Fe XI]/F_x ratios, which involve only 14 data points, the uncertainty is ±0.15). Refer to the null hypothesis probabilities in Table 3 to assess whether these correlations are real.

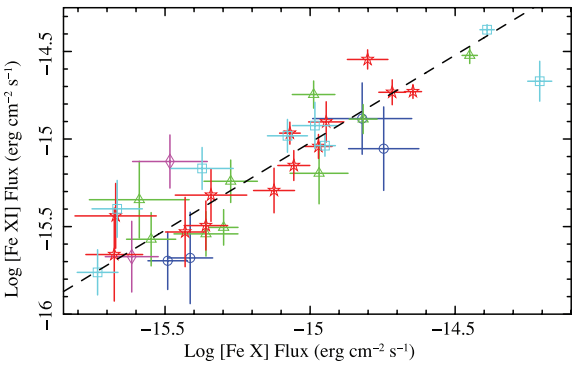

Figure 6. Fluxes of [Fe XI] and [Fe X]. The dashed line represents the average [Fe XI]/[Fe X] ratio, 0.95. Only two sample members have ratios that differ from this by $>2.3\sigma$. Point styles are the same as in Fig. 3.

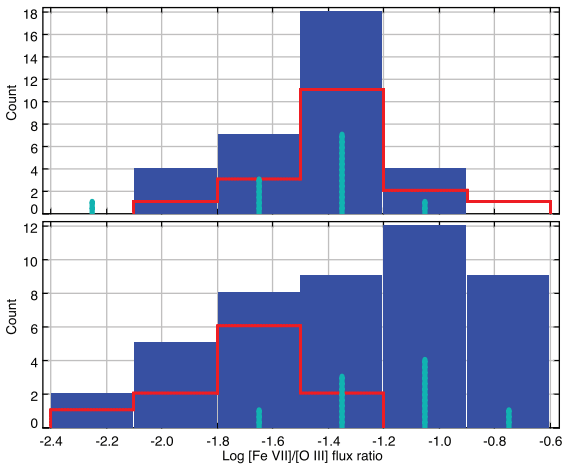

Figure 7. Distributions of [Fe VII]$_T$/[O III]$_T$ flux ratios amongst NLS1, BLS1 and Sy2 populations in the [Fe X]-selected and NTM00 samples (upper and lower panels, respectively). In contract with NTM00, we find no significant difference between the BLS1 and Sy2 distributions.

4.3 Line profiles

The widths and velocity shifts (v_{sh}) of the best-fitting line components are summarized in Table 5 for both the overall sample and subsets defined by Seyfert spectral classification. Note that [Fe XI] and [Fe VII]$_W$ are included in only some of the final models. Consequently, the values of these parameters are more strongly affected by small number statistics, especially for some subsamples, and should be interpreted with caution. Likewise, there are only three Sy1.9s so the typical line properties of this class of Seyfert are not very well constrained; their average best-fitting parameters have large uncertainties and are consistent with those of both the Sy1.5s and the 2.0s. We therefore exclude Sy1.9s from Table 5. Caution is

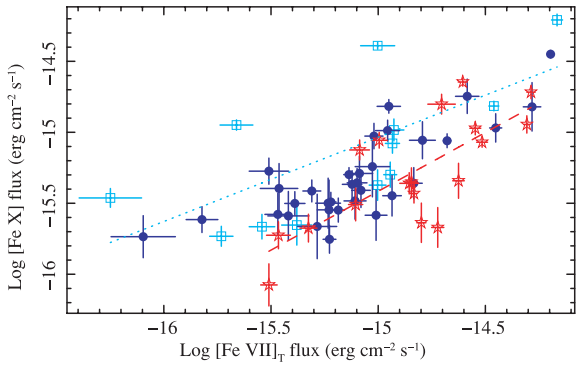

Figure 8. [Fe X] versus [Fe VII]$_T$ flux. Blue filled circles are BLS1s (Sy1.0, 1.5 and 1.9), cyan open squares are NLS1s and red stars are Sy2s; the cyan dotted line is a linear regression fitted to the NLS1s and the red dashed line is a line fitted to the Sy2s. The distributions of NLS1s and Sy2s overlap, but the [Fe X]/[Fe VII]$_T$ ratios of the NLS1s are systematically higher than those of the Sy2s: not one NLS1 lies below the line fitted to the Sy2s.

also advised when comparing lines fitted with different models, as this can introduce systematic effects. To facilitate the comparison of [Fe VII] with higher ionization FHILs, we include statistics for the best-fitting single-Gaussian models, [Fe VII]$_{1G}$, as well as the double-Gaussian components.

Several things may be demonstrated with the average profile properties in Table 5. We find that the cores of lines with the lowest IPs have velocity shifts that are generally consistent with [S II], whilst the wings of [O III] tend to be outflowing. The [Fe VII] profiles are characterized by blue cores and sometimes include even bluer wings. The most blueshifted lines are found in our highest IP feature, [Fe XI]. The widths of the line cores and single-Gaussian line models increase monotonically with critical density, with [Fe XI] exhibiting the broadest lines. Thus, we reaffirm earlier studies that found a tendency for the linewidth and blueshifts to increase with increasing IP (e.g. Appenzeller & Öestreicher 1988). Moreover, the FHIL profiles are quantitatively similar to previous results. According to Erkens et al. (1997), the average FWHM ratios of the FHILs over [O III] are 1.63, 1.58 and 1.86, respectively, for the [Fe VII]/[O III], [Fe X]/[O III] and [Fe XI]/[O III] width ratios; we obtain values of 1.60, 1.60 and 2.04 for the width ratios of [Fe VII]$_{1G}$, [Fe X] and [Fe XI] over [O I] (here we use [Fe VII]$_{1G}$ and [O I] instead of [Fe VII]$_C$ and [O III]$_C$ to be consistent in using single-Gaussian models). Comparing the different Seyfert types, we find that the NLS1s tend to have the highest FHIL outflow velocities, whilst the Sy2s tend to have the narrowest FHILs.

In Table 6, we present the correlation statistics between the line profile parameters of various emission features. These statistics show that the velocity shift correlations between the FHILs are universally stronger than those between any other pair of features.

Table 5. Average parameters of fitted line profiles.

Line model	Overall mean (rms)	NLS1 mean (rms)	Sy1.0 mean (rms)	Sy1.5 mean (rms)	Sy2 mean (rms)
		Line velocities measured relative to [S II] (v_{sh}, km s^{-1})			
[O III]$_C$	−5 ± 5 (40)	−8 ± 6 (21)	−8 ± 6 (22)	−15 ± 13 (50)	12 ± 11 (47)
[O III]$_W$	−134 ± 19 (147)	−112 ± 30 (100)	−65 ± 24 (87)	−134 ± 57 (221)	−196 ± 29 (121)
[O I]	0 ± 4 (30)	7 ± 7 (23)	−1 ± 6 (20)	−2 ± 12 (46)	2 ± 5 (21)
[Fe VII]$_C$	−74 ± 16 (128)	−99 ± 41 (136)	−54 ± 28 (101)	−93 ± 42 (163)	−44 ± 25 (103)
[Fe VII]$_C$[a]	−296 ± 28 (102)	−331 ± – (–)	−213 ± 63 (63)	−305 ± 63 (63)	−308 ± 42 (118)
[Fe VII]$_{1G}$	−86 ± 16 (126)	−100 ± 41 (135)	−57 ± 27 (99)	−95 ± 42 (162)	−83 ± 25 (102)
[Fe X]	−84 ± 18 (143)	−128 ± 44 (147)	−39 ± 36 (130)	−107 ± 44 (171)	−61 ± 30 (124)
[Fe XI][a]	−212 ± 32 (192)	−258 ± 39 (103)	−41 ± 19 (33)	−217 ± 76 (216)	−186 ± 52 (181)
Hα_N	−34 ± 11 (85)	−69 ± 21 (68)	−27 ± 33 (120)	−32 ± 24 (93)	−22 ± 13 (52)
Hα_B	−3 ± 26 (206)	52 ± 21 (71)	−6 ± 70 (253)	24 ± 57 (222)	–
		Linewidths (FWHM; km s^{-1})			
[S II]	322 ± 12 (90)	284 ± 22 (73)	314 ± 24 (88)	330 ± 25 (98)	346 ± 23 (90)
[O III]$_C$	319 ± 12 (96)	267 ± 14 (48)	315 ± 17 (63)	363 ± 36 (140)	316 ± 19 (80)
[O VII]$_W$	779 ± 33 (257)	801 ± 59 (196)	758 ± 48 (175)	777 ± 77 (298)	798 ± 72 (296)
[O I]	380 ± 20 (154)	299 ± 21 (70)	354 ± 19 (70)	437 ± 55 (213)	404 ± 41 (169)
[Fe VII]$_C$	500 ± 29 (230)	502 ± 74 (245)	489 ± 53 (190)	561 ± 60 (234)	433 ± 57 (236)
[Fe VII]$_W$[a]	860 ± 91 (327)	652 ± – (–)	696 ± 357 (357)	459 ± 279 (279)	1009 ± 94 (267)
[Fe VII]$_{1G}$	571 ± 29 (230)	507 ± 73 (241)	526 ± 43 (156)	567 ± 59 (227)	645 ± 64 (263)
[Fe X]	556 ± 32 (251)	591 ± 73 (241)	508 ± 35 (125)	690 ± 84 (326)	447 ± 56 (231)
[Fe XI][a]	643 ± 65 (383)	864 ± 176 (467)	463 ± 104 (180)	749 ± 161 (455)	488 ± 78 (272)
Hα_N	415 ± 20 (157)	335 ± 29 (95)	405 ± 25 (91)	498 ± 57 (219)	406 ± 35 (143)
Hα_B	3475 ± 273 (1949)	1515 ± 150 (498)	4718 ± 523 (1887)	4491 ± 377 (1458)	–
		Model counts			
Most features	63	12	14	16	18
[Fe VII]$_W$	14	1	2	2	9
[Fe XI]	36	8	4	9	13

[a]Statistics are limited (especially for some spectral types) because not all final models include [Fe VII]$_W$ and [Fe XI].
Forbidden lines are listed in the order of increasing N_{cr}. Columns are (1) line model component; (2–6) average value ± the 1σ statistical uncertainty of mean and the rms distribution (in parentheses) of model parameters for overall sample and subsets of each spectral type; (2) all Seyfert types, including Sy1.9s; (3) NLS1; (4) Sy1.0; (5) Sy1.5; (6) Sy2. Sy1.9s are not presented because there are only three in our sample (two with detected [Fe XI], none with [Fe VII]$_W$), so the average model parameters are not very well constrained. The Sy1.9 averages are consistent with those of both Sy1.5s and Sy2s.

Table 6. Correlation statistics of the line profile parameters of selected emission lines.

	[O I]	Hα_N	[O III]$_C$	[O III]$_W$	[Fe VII]$_{1G}$	[Fe VII]$_C$	[Fe X]	[Fe XI]
				Line v_{sh} correlation statistics				
[O I]	–	–	0.621 (−7.2)	0.469 (−4.0)	0.390 (−2.8)	0.318 (−2.0)	0.330 (−2.1)	0.508 (−2.8)
Hα_N	–	–	0.321 (−2.0)	0.162 (−0.7)	0.315 (−1.9)	0.344 (−2.2)	0.341 (−2.2)	0.156 (−0.4)
[O III]$_C$	0.621 (−7.2)	0.321 (−2.0)	–	0.237 (−1.2)	0.445 (−3.6)	0.473 (−4.0)	0.302 (−1.8)	0.397 (−1.8)
[O III]$_W$	0.469 (−4.0)	0.162 (−0.7)	0.237 (−1.2)	–	0.367 (−2.5)	0.255 (−1.4)	0.308 (−1.9)	0.391 (−1.7)
[Fe VII]$_{1G}$	0.390 (−2.8)	0.315 (−1.9)	0.445 (−3.6)	0.367 (−2.5)	–	–	0.681 (−9.1)	0.754 (−7.0)
[Fe VII]$_C$	0.318 (−2.0)	0.344 (−2.2)	0.473 (−4.0)	0.255 (−1.4)	–	–	0.697 (−9.7)	0.702 (−5.7)
[Fe X]	0.330 (−2.1)	0.341 (−2.2)	0.302 (−1.8)	0.308 (−1.9)	0.681 (−9.1)	0.697 (−9.7)	–	0.761 (−7.1)
[Fe XI]	0.508 (−2.8)	0.156 (−0.4)	0.397 (−1.8)	0.391 (−1.7)	0.754 (−7.0)	0.702 (−5.7)	0.761 (−7.1)	–
				Line FWHM correlation statistics				
[O I]	–	–	0.810 (−15.1)	0.539 (−5.3)	0.460 (−3.8)	0.356 (−2.4)	0.163 (−0.7)	0.196 (−0.6)
Hα_N	–	–	0.829 (−16.3)	0.567 (−5.9)	0.483 (−4.2)	0.352 (−2.3)	0.259 (−1.4)	0.331 (−1.3)
[O III]$_C$	0.810 (−15.1)	0.829 (−16.3)	–	0.693 (−9.5)	0.422 (−3.2)	0.242 (−1.3)	0.312 (−1.9)	0.332 (−1.3)
[O III]$_W$	0.539 (−5.3)	0.567 (−5.9)	0.693 (−9.5)	–	0.331 (−2.1)	0.047 (−0.1)	0.099 (−0.4)	0.132 (−0.4)
[Fe VII]$_{1G}$	0.460 (−3.8)	0.483 (−4.2)	0.422 (−3.2)	0.331 (−2.1)	–	–	0.411 (−3.1)	0.605 (−4.0)
[Fe VII]$_C$	0.356 (−2.4)	0.352 (−2.3)	0.242 (−1.3)	0.047 (−0.1)	–	–	0.457 (−3.8)	0.588 (−3.8)
[Fe X]	0.163 (−0.7)	0.259 (−1.4)	0.312 (−1.9)	0.099 (−0.4)	0.411 (−3.1)	0.457 (−3.8)	–	0.773 (−7.5)
[Fe XI]	0.196 (−0.6)	0.331 (−1.3)	0.332 (−1.3)	0.132 (−0.4)	0.605 (−4.0)	0.588 (−3.8)	0.773 (−7.5)	–

Note. The Spearman rank correlation coefficient (ρ) and the log of the null hypothesis probability (in parentheses) for the profile parameters of selected emission lines. Statistics are based upon the full [Fe X]-selected sample with the exception of [Fe XI] correlations, which use only the 36 [Fe XI] detections. Hα_B is omitted from the table because it was not found to correlate significantly with any of these parameters; its FWHM exhibits no correlations with confidence above the 90 per cent level, whilst its velocity showed no correlations with even 50 per cent confidence. [Fe VII]$_W$ is omitted because it is only applied to 14 sample members so the confidence levels of its correlations are low; its only correlation found to have >99 per cent confidence is between the FWHM values of [Fe VII]$_W$ and [O III]$_W$. We do not report correlations between the profiles of [O I] and Hα_N and between [Fe VII]$_{1G}$ and [Fe VII]$_C$ because these models are often constrained to have the same profiles; in particular these [Fe VII] models are identical in all but 14 instances. As with Table 3, the values are repeated in the upper-right and lower-left halves of these tables for convenience.

On the other hand, with the exception of the [Fe XI]–[Fe X] pair, the strongest linewidth correlations are found amongst the low-IP features.

The profiles of [Fe X] and [Fe XI] are mutually consistent for much of the sample, but a subset of the [Fe XI] lines appears to be both broader and bluer (Fig. 9a and b). The velocity shifts are almost always negative, indicating that the emitting clouds are outflowing. The v_{sh} values are consistent for roughly half of the sample, whereas the [Fe XI] outflow velocities are significantly faster in roughly one-third of the sources ([Fe XI] is faster in 11 out of 36 sources with at least 3σ confidence). In no instance is [Fe XI] significantly slower. Overall, the average velocity shift difference is v_{sh} ([Fe XI]) − v_{sh} ([Fe X]) = −109 km s^{-1} with an rms scatter of 126 km s^{-1}. The widths of the [Fe XI] lines tend to be either consistent with or broader than [Fe X] (Fig. 9b), although the FWHM values are not as well constrained as v_{sh}. For both ionic species, the fastest outflow velocities are found amongst the broadest lines (although the broadest lines do not always have fast v_{sh} values).

Unlike [Fe XI], there is no tendency for the [Fe VII]$_{1G}$ models to have different widths or velocity shifts from those of [Fe X] (Fig. 10). The average velocity shift difference is effectively zero with somewhat less scatter [v_{sh} ([Fe X]) − v_{sh} ([Fe VII]$_{1G}$) = 5 km s^{-1} with rms = 108 km s^{-1}]. Likewise, there is no significant difference between the widths of [Fe VII]$_{1G}$ and [Fe X]. However, in contrast to v_{sh}, the correlation of the linewidths is weaker and lower confidence.

Amongst the lower IP features, the only lines or line components that tend to be in outflow are the wings of [O III]. At best, the velocity shifts of [O III]$_W$ and the FHILs are weakly correlated (only [Fe VII]$_{1G}$ appears to correlate with greater than 99 per cent confidence). However, as noted in Section 3.2.3, there is a degeneracy in the process of separating the core and wing

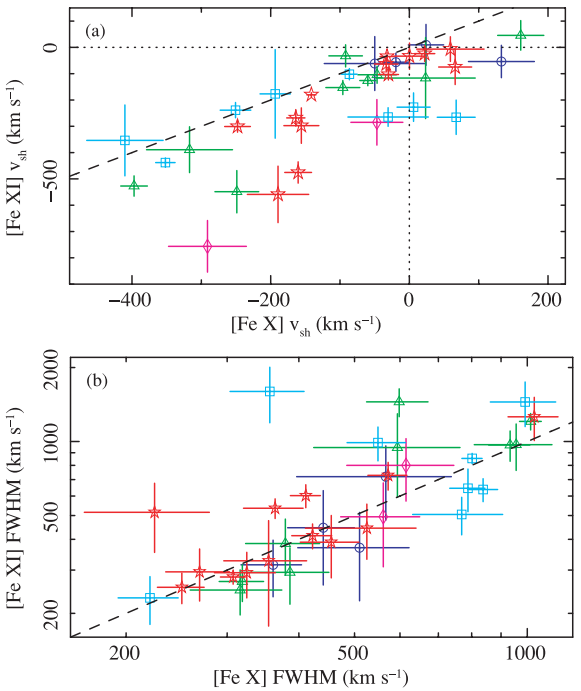

Figure 9. Velocity shifts (a) and FWHM (b) of [Fe XI] and [Fe X]. Point shapes and colours are the same as Fig. 3. Dashed $x = y$ lines are included to guide the eye. Most [Fe X] and [Fe XI] lines appear to be outflowing (v_{sh} < 0 km s^{-1}). In a little more than half the sample, the v_{sh} values are consistent; in the remaining cases, the outflow velocities of [Fe XI] are faster (by up to 300 km s^{-1}). The FWHM values of [Fe XI] tend to be either as broad or broader than those of [Fe X], but the linewidth uncertainties are large.

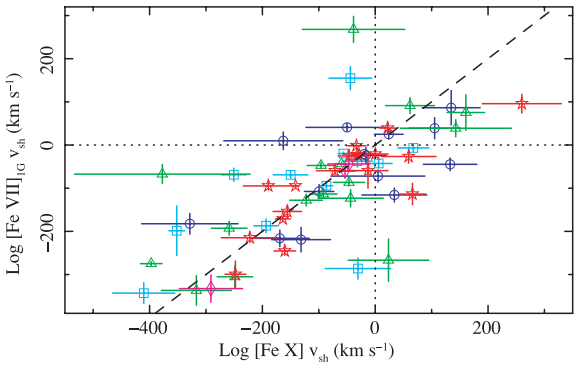

Figure 10. Velocity shifts of [Fe VII]$_{1G}$ and [Fe X]. A dashed $x = y$ line is sketched to guide the eye. Point shapes and colours are the same as Fig. 3. Unlike the v_{sh} values of [Fe XI] (Fig. 9a), there is no tendency for the [Fe VII]$_{1G}$ lines to be more or less shifted than [Fe X]. The scatter in this plot is dominated by a few data points with large [Fe X] v_{sh} uncertainties.

component models that introduces additional uncertainties in these component parameters, possibly causing systematic effects and certainly increasing the noise. We therefore interpret the [O III]$_W$ parameters with caution. It is true that the measured [O III]$_W$ outflow velocities tend to be higher than those of [Fe VII]$_C$, [Fe VII]$_{1G}$ and [Fe X], but this may be an artefact of the deblending process. What is clear is that [O III] has (at least) two components, the broader of which is outflowing whilst the narrower one is not shifted relative to the lower ionization species, such as [S II] and [O I]. The fact that the measured [O III]$_W$ velocity shifts are not much larger than those of the FHILs leaves open the possibility that this component may be kinematically related to the FHIL-emitting region.

4.4 X-ray properties

In Fig. 11, we show the correlation between [Fe X] and 0.1–2.4 keV fluxes amongst the 32 sample members with *ROSAT* detections. The [Fe X] intensities of the type 1 Seyferts (1.0, 1.5 and NLS1) scale with power in the X-ray band, consistent with the trend shown by Porquet et al. (1999; fig. 2; represented here in Fig. 11 by the diagonal dashed line). The only three *ROSAT*-detected Sy2s have

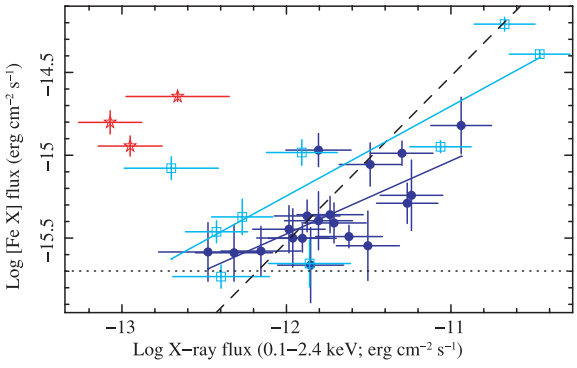

Figure 11. [Fe X] versus X-ray flux in the full *ROSAT* band (0.1–2.4 keV). Point styles are the same as in Fig. 8. The solid diagonal lines are linear correlations fitted to the NLS1 (higher, cyan line) and BLS1 (lower, blue line) populations. The horizontal dotted line at $F_{[\mathrm{Fe\,X}]} = 2 \times 10^{-16}$erg cm^{-2} s^{-1} is the approximate flux limit of [Fe X] in our sample. The black dashed line indicates a constant ratio of [Fe X]/X-ray $= 3 \times 10^{-4}$, which is representative of the flux ratios shown by Porquet et al. (1999). Apart from the Sy2s, which are likely affected by X-ray absorption, the highest [Fe X]/X-ray ratios are generally NLS1s.

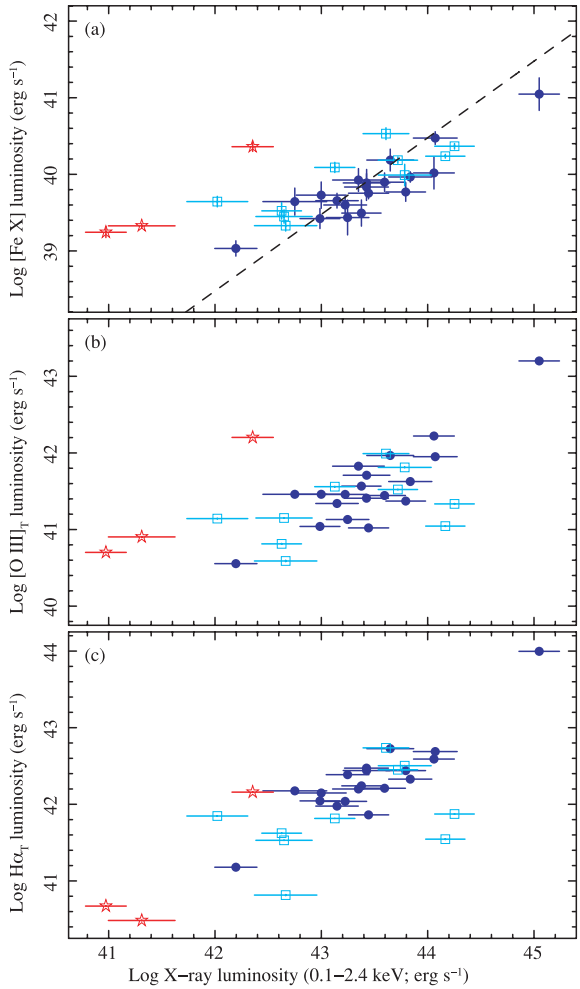

Figure 12. Luminosities of [Fe X], [O III]$_T$ and Hα_T (panels a–c, respectively) versus L_x in the observed 0.1–2.4 keV band. Point styles and the dashed line are as in Fig. 11 (the error bars for [O III]$_T$ and Hα_T are smaller than the points). Panels a and b demonstrate that the line and X-ray powers of type 1 Seyferts are correlated, but the Sy2s are offset by more than an order of magnitude in L_x; in panel c, the Sy2s, whose Hα_T lines lack a broad component, lie closer to the type 1 objects. An inspection of the type 1 Seyferts shows that the relationships of [O III]$_T$ and Hα_T with L_x exhibit more scatter than [Fe X], although in the case of Hα_T the additional scatter is primarily due to a few outliers (see Section 5.4). We note that whilst these plots are affected by the Malmquist bias, they still offer a fair representation of the relative amounts of scatter amongst the different correlations.

by far the highest [Fe X] /X-ray ratios, by roughly a factor of 30 over the type 1 Seyferts. Moreover, as demonstrated by the plot of [Fe X] and X-ray luminosities (Fig. 12, upper panel), they also have some of the lowest observed X-ray powers. This is readily interpreted within the Seyfert unification framework (e.g. Antonucci 1993) as obscuration along the line of sight to the X-ray emitting regions of the type 2 systems. If such obscuration also affects our view of the FHIL-emitting clouds, then it must cover only a fraction of this region as these sources are detected by their [Fe X] lines.

The lower IP lines do not correlate as tightly with X-ray power. This is illustrated by Fig. 12, which plots the luminosities of [Fe X], [O III]$_T$ and Hα_B against L_x. Amongst the type 1 Seyferts, the correlations are all positive, but with differing amounts of scatter: [Fe X] has the least (the rms scatter about the mean [Fe X]/F_x ratio is 0.38 dex), followed by [O III]$_T$ (0.45 dex) and Hα_T (0.48 dex;

see the last column of Table 4 for the rms scatter of other lines with F_x; see also Fig. A5). It is worth noting that of all the measured lines, [Fe VII]$_T$ exhibits the weakest correlation with F_x with a larger rms than any other line. We note further that the scatter in the Hα_T versus X-ray plot (bottom panel of Fig. 12) is dominated by a few outliers; if we disregard the three NLS1s with the lowest Hα_T/X-ray ratios, the correlation becomes marginally stronger and tighter than that of [Fe X] ($\rho = 0.667$ with an rms scatter of 0.34 dex).

5 DISCUSSION

5.1 Line profiles, IPs and FHIL kinematics

The [Fe X] and [Fe XI] lines are expected to be well correlated because they have similar IPs (234 and 262 eV, respectively) and $N_{cr}(10^{9.7}$ and $10^{10.4}$ cm$^{-3})$. Indeed, we find that their fluxes are essentially indistinguishable (Section 4.2), and they have mutually consistent profiles in more than half of the sample members with [Fe XI] detections. However, in the remaining sources the [Fe XI] lines tend to be both broader and bluer than [Fe X]. This suggests that the distribution of [Fe XI]-emitting clouds sometimes extends closer to the BLR, probing a region where the outflow velocities are higher. Similar evidence has been shown for selected objects in smaller samples (e.g. Erkens et al. 1997; Mullaney & Ward 2008).

The velocity shifts of [Fe VII]$_{1G}$ are similar to, and well correlated with, those of [Fe X], suggesting that the clouds responsible for the core of the [Fe VII] profile are part of the same flow as the [Fe X]-emitting clouds. However, there is only a weak correlation between the widths of these components. It is therefore unlikely that the [Fe VII]$_{1G}$ and [Fe X] lines are dominated by the same clouds. An alternative hypothesis is that they are from spatially distinct regions of an outflow that is 'coasting', neither accelerated nor decelerated significantly between the [Fe X]- and [Fe VII]-emitting portions of the flow. In such a scenario, the [Fe VII] clouds are expected to be the downstream component due to the lower ionization parameter required and may be more readily resolved spatially. This is consistent with our recent photoionization models of FHIL emission in the NLS1 Ark 564, from which we infer that clouds in a radiatively driven outflow are accelerated before the FHIL becomes strong. The terminal velocity is approached and Fe is released within the clouds as dust grains become sublimated (Mullaney et al. 2009). We note further that the wings of [O III] are outflowing and may be related to the [Fe X]- and/or [Fe VII]$_{1G}$-emitting portion of the outflow, as the average [O III]$_W$ velocity shifts amongst the NLS1s, Sy1.0s and Sy1.5s are consistent with those of these FHILs (cf. Section 4.3). On the other hand, the velocity shifts of [O III]$_C$ and the lower ionization narrow lines are consistent with that of [S II] and are not part of this flow.

5.2 Line correlations with X-rays

In Section 4.4, we show that the [Fe X] lines of type 1 Seyferts scale rather well with X-ray flux, in agreement with previous studies (Porquet et al. 1999). However, we note a systematic difference between the NLS1 and BLS1s. This is made clear by the offset between the linear correlations fitted to these two populations in Fig. 11. One contributor to this is likely to be our simplistic assumption of a uniform spectral model to convert *ROSAT* count rates to fluxes. NLS1s have long been known to have, on average, stronger soft excess and steeper soft X-ray spectra (e.g. Boller 2000). If we adopt a steeper spectral index for these objects ($\Gamma = 3.0$ instead of 1.5) and plot [Fe X] flux against just the estimated 233–300 eV flux (which dominates the photoionization of [Fe X] and [Fe XI]), the offset between the NLS1 and BLS1 distributions disappears (Fig. 13). Thus, it appears that a single correlation between the [Fe X] and soft X-ray fluxes applies to both NLS1s and BLS1s. It follows that observations of coronal lines may be used to constrain the spectral energy distribution (SED) at soft X-ray energies when observations in this band are either not available or of low sensitivity. The average ratio we obtain for $\log([\mathrm{Fe\,X}]/F_{233-300\mathrm{eV}})$ is -2.03 ± 0.07 with an rms of 0.36. Additionally, we note that the NLS1 and BLS1 distributions are not as clearly separated in the [O III]$_T$–L_x or Hα_T–L_x planes (Fig. 12b and c). Inaccuracies in the assumed spectral indices of NLS1s should have a smaller effect upon these correlations because, unlike [Fe X], the [O III]$_T$ and Hα_T line emission is not particularly responsive to any specific portion of the X-ray band. Consequently, they should scale more directly with the bolometric power, hence the overall *ROSAT* luminosity, the estimate of which is less sensitive to the model used to interpret PSPC count rates.

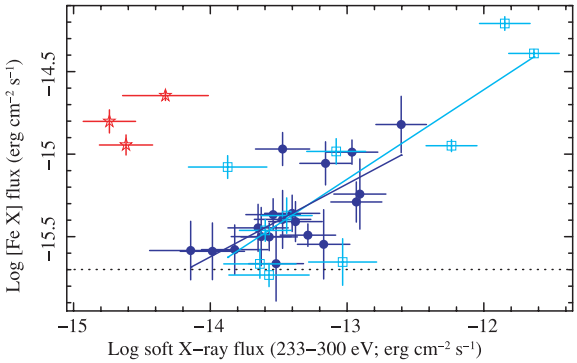

Figure 13. [Fe X] versus soft X-ray flux. The soft band is the portion of the X-ray spectrum most directly responsible for photoionizing [Fe X]. Here, we estimate the 233–300 keV flux with the further assumption that NLS1s have a softer X-ray spectrum ($\Gamma = 3.0$). As a result, the difference between the [Fe X] /X-ray ratios of NLS1s and BLS1s essentially disappears (compare to Fig. 11). This is demonstrated by the linear correlations fitted to these two populations (cyan and blue solid lines, respectively). The horizontal dashed line is once again the approximate [Fe X] flux limit and the point styles are the same as in Fig. 11.

The amount of scatter in the emission line versus X-ray correlations allows us to put constraints on the size of the line-emitting regions and the variability history of the AGN. In principle, the lines should scale with the bolometric power of the central engine, hence they should correlate with the X-ray flux. However, any variability of the photoionizing continuum strength will weaken the observed correlation because the *ROSAT* data provide a snapshot of the AGN power at a moment in time, whereas the line-emitting regions are extended and therefore the observed lines are a response to the AGN power averaged over the light-crossing time of these regions. The more variable the bolometric power is, on time-scales much shorter than either the light-crossing time of the line-emitting regions or the time lag between the X-ray and optical spectroscopic observations, the more likely it becomes that the instantaneous X-ray power observed would not be representative of the time-averaged power affecting the measured lines. The relatively modest scatter found amongst the type 1 Seyferts in Fig. 13 (0.38 dex) indicates that the instantaneous X-ray power measured by *ROSAT* was within a factor of a few of the time-averaged power to which the FHILs were responding when observed by SDSS 10–15 years later. Thus, none

of our sources appears to have been caught in a short time-scale X-ray fluctuation at the time of the *ROSAT* observation, or a several-year drift in power since that time, by more than a factor of a few. A contribution to the scatter in the emission line versus X-ray plots is the made by the model dependence inherent in converting *ROSAT* count rates to fluxes, which in the most extreme cases could introduce F_x errors up to a factor of 2. We note that the scatter exhibited by the NLS1 is much larger than that of the BLS1 distribution in Fig. 13 (0.48 versus 0.27 dex). This could be due to either variability or greater inaccuracies in the models used to interpret the count rates, as NLS1s are known both to be more variable and to exhibit a wider range of spectral indices in the soft X-ray band.

The fact that the correlation between [Fe VII]$_T$ and X-rays is weaker with much more scatter than that between [Fe X] and X-rays suggests that the [Fe VII]-emitting clouds are much more extended than those of [Fe X]. The longer light-crossing time of a more extended region gives the central engine more time to drift away from the time-averaged power to which the [Fe VII] line is responding. Other sources of noise in this correlation are less likely because (1) there is not likely to be much photoionized [Fe VII] emission that is unrelated to the AGN because the stellar continuum power above the IP energy of 99 eV is negligible and (2) the correlation between the velocities of [Fe VII]$_{1G}$ and [Fe X] (Fig. 10) connects the [Fe VII]-emitting clouds to the [Fe X]-bearing outflow, demonstrating that the [Fe VII]-emitting medium likely originates in the AGN and showing no sign of the deceleration that would take place if this flow were shocked. Furthermore, the similarity of the [Fe VII]–X-ray correlation to those between various narrow lines and X-rays, and the strong correlations between [Fe VII] and the NLR lines (notably [O I] and [O III]) suggest that the [Fe VII]-emitting region merges with that of the traditional NLR. This is corroborated by previous studies which have shown that unlike coronal lines with higher IPs and N_{cr}, the measured profiles of [Fe VII] are often consistent with those of the lower ionization forbidden lines (Veilleux 1991).

5.3 Structure of the FHIL-emitting region

What is the geometry of the FHIL-emitting region of Seyfert galaxies? MT98 found that amongst a sample of 35 Seyferts mostly collected from the literature, type 2 Seyferts have significantly lower [Fe VII]/[O III] flux ratios than type 1s, suggesting that at least part of the [Fe VII]-emitting region is obstructed along our line of sight in Sy2 galaxies. From this they infer that some of the [Fe VII] emission arises from regions hidden from our view by the same structure that obscures the BLR in Sy2s, the circumnuclear torus. NTM00 reaffirm this result using an expanded sample (Fig. 7) and report a similar, albeit weaker, disparity in the distributions of [Fe X]/[O III] ratios, therefore concluding that the [Fe X]-emitting clouds are less obscured than those responsible for the [Fe VII] emission. These authors therefore argue that a significant fraction of the [Fe VII] flux arises from a material at the inner surface of the torus, whereas a larger fraction of the [Fe X] emission arises from a larger scale region. On the other hand, several other authors have interpreted the correlation between critical densities, IPs and the width of the line profiles as evidence for a stratified line-emitting region in which the clouds responsible for the FHILs extend from the outer reaches of the BLR through the NLR, with the highest ionization lines arising closest to the BLR (De Robertis & Osterbrock 1984, 1986; Appenzeller & Öestreicher 1988; Rodríguez-Ardila et al. 2002).

As described in Section 4.2, we do not find any significant difference between the [Fe VII]/[O III] ratios of types 1 and 2 Seyferts, in contradiction with MT98 and NTM00. We do find that the

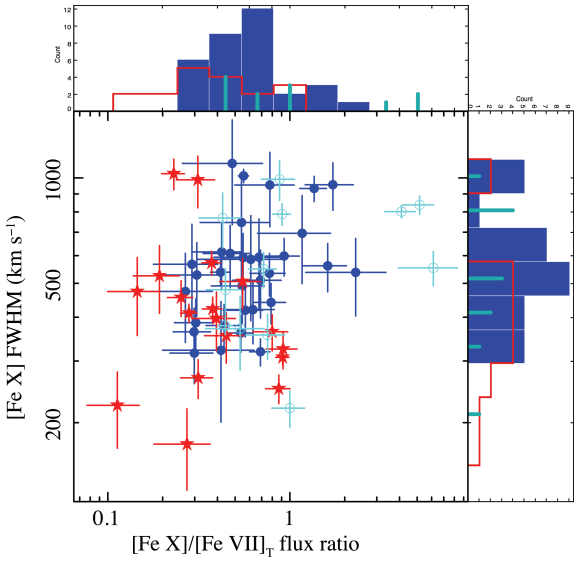

Figure 14. [Fe X] linewidth versus [Fe X]/[Fe VII]$_T$ flux ratio. Point styles as in Fig. 8; histogram styles as in Fig. 4 (top panel). The Sy2s on average have less [Fe X] power per unit of [Fe VII] power than either the BLS1s or the NLS1s, although the histogram at the top demonstrates that the distributions are broad with substantial overlap. The histogram at right shows that the [Fe X] lines tend to be narrower in Sy2s. Taken together, these suggest that a part of the [Fe X]-emitting region, the part that contributes the broadest line flux, is often hidden from us in Sy2s.

[Fe X]/[Fe VII]$_T$ [10] ratios differ between the spectral types, but these differences are the opposite of what would be expected from the NTM00 results. The mean averages of the log ratios we obtain are 0.03 ± 0.13, -0.24 ± 0.04 and -0.44 ± 0.06 for NLS1s, BLS1s and Sy2s, respectively. There is considerable overlap in the distributions (see the histogram at the top of Fig. 14), but the probability that the NLS1s and Sy2s are drawn from populations with the same ratio distribution is less than 0.001 per cent according to a KS test. The interpretation of these differences could be either an excess of [Fe VII] or a deficiency of [Fe X] amongst Sy2s and the opposite situation amongst NLS1, as will be discussed below. Note, however, that the average ratio of the NLS1s is increased significantly by three outliers with $\log([\text{Fe X}]/[\text{Fe VII}]) > 0.6$. If these extreme sources are omitted, the mean ratio amongst the remaining nine NLS1s (-0.19 ± 0.05) is consistent with that of the BLS1s. Thus, the NLS1s may represent a heterogeneous population that includes some objects with rather extreme properties and some that more closely resemble BLS1s.

Differences between the best-fitting [Fe X] model parameters of types 1 and 2 Seyferts provide evidence that the low [Fe X]/[Fe VII] ratios amongst Sy2s is due to partially obscured [Fe X] emission. In Sy2s, these lines tend to be narrower and have lower fluxes relative to [Fe VII] (Fig. 14). This is consistent with a scenario in which the part of the [Fe X]-emitting region that contributes the broadest line flux generally cannot be observed in Sy2 galaxies, and in which the [Fe VII]-emitting region is less affected by obscuration.

[10] Here, we discuss [Fe X]/[Fe VII] ratios instead of Fe line/[O III] to mitigate two factors: (1) the effect of reddening, for which we have not corrected, is less than 10 per cent for this ratio (Section 3.2.6) and (2) any bias of the present [Fe X]-selected sample in favour of high FHIL/non-FHIL ratios (Section 4.2). However, the [Fe X]/[O III] ratios show similar tendencies as [Fe X]/[Fe VII].

5.4 NLS1s with extreme [Fe X]/[O III] ratios

In the preceding sections, it was noted that a few NLS1s have extreme line ratios that cause them to stand out from both the other NLS1s and the other sample members in general (see Figs 8 and 12 and the discussion of [Fe X]/[Fe VII] flux ratios in Section 5.3). Two NLS1s in particular, Sources 25 and 50, are consistently the most extreme outliers whenever there are outliers to a correlation. For instance, these are the only two sample members with $\log([\mathrm{Fe\,X}]/[\mathrm{O\,III}]_T) > -1.0$, whereas the mean for the rest of the sample is -1.66 ± 0.04 with an rms = 0.28. In addition to their extreme line ratios, these sources have two of the narrowest Hα_B lines in our sample (FWHM values of 745 ± 2 and 780 ± 2 km s^{-1}, respectively). What is it about these NLS1s that sets them apart from the rest of the sample?

Not every pair of correlated parameters has significant outliers. For instance, there are no outliers in the [Fe X]–[Fe XI] plane (Fig. 6) nor if we plot [O I] versus $[\mathrm{O\,III}]_T$ (Fig. A1a). As discussed earlier, [Fe X] and [Fe XI] emission lines both respond to the continuum in the soft X-ray band. We therefore expect these three fluxes to be closely correlated. This is found to be the case for the present sample, without exception. Likewise, we do not find any obvious outliers when we compare fluxes of pairs of NLR features (such as [O III], [O I], [N II] or Hα_N). It is only when we compare fluxes between these two groups that the outliers tend to stand out, with high ratios of [Fe X] (or [Fe XI] or X-rays) over NLR fluxes. These groups may be thought of as compact and extended emission regions, or as high- and low-energy processes.

It appears that for the two consistent outliers the relationship between the smaller scale/higher energy processes and the larger scale/lower energy features differs from that of most other Seyferts. Two possible causes for this disconnect are variability and differences in the broad-band spectral shapes. If the average power of the AGN has changed relatively recently (10–100 years or so), then the compact FHIL-emitting region will have had time to respond but the more extended NLR will not. Alternatively, these outliers may be affected by a broad-band spectral feature that is not present (or as prominent) in other sample members. Erkens et al. (1997) have suggested that AGN with strong excesses in the soft X-ray band tend to produce strong FHILs, based upon the correlation they demonstrated between the [Fe X] equivalent widths and the photon index of *ROSAT* data. An extreme soft excess would provide a disproportionate supply of ∼250 eV photons, thereby producing extra FHIL emission through photoionization; lines that respond to other parts of the continuum will not be affected so their relative strength will be lower. It is worth noting that one of these outliers is KUG 1031+398, which has one of the strongest soft excesses known[11] (Puchnarewicz et al. 2001; Middleton, Done & Gierliński 2007). We note further that the two outliers have the lowest HR1 values of all the RASS-detected members of the sample (HR1 = hardness ratio for the low-energy end of the *ROSAT* band), suggesting that Source 50 may also have a strong soft excess.

The observation that both of our consistent outliers may have strong excesses in the soft X-ray band is suggestive that the mechanism that causes them to stand out relates to the SED shape, but with just two objects this does not rule out the possibility that these sources stand out due to variability. To break the degeneracy between an origin relating to the scale size and one relating to the SED, we consider Hα_B. The BLR is more compact than the FHIL-emitting region, but Hα emission is not specifically sensitive to the soft X-ray continuum. In Fig. 12c, the two data points farthest from the Hα_T–L_x correlation are Sources 25 and 50, whereas Fig. A3b shows that there are no egregious outliers in the $[\mathrm{O\,III}]_T$–Hα_T plane.[12] Thus, the Hα_B emission in these objects tracks with the larger scale/lower energy features and not the smaller scale/higher energy features, indicating that Sources 25 and 50 behave differently from most of the sample due to a difference in their SEDs, not variability.

If Sources 25 and 50 do have strong soft excesses, and if this feature of their SED affects the emission lines, then we can use the emission lines to constrain portions of the soft excess that are difficult to observe directly. Specifically, we can use the strength of [Fe VII] relative to other features to constrain the photoionizing continuum around 100 eV. We find that these sources are outliers in the [Fe VII]–[Fe X] flux plane (Fig. 8) but not in the [Fe VII]–[O III] plane (Fig. A2c). Thus, it appears that the [Fe VII] lines do not respond strongly to the soft excess: either this spectral component does not extend down to 100 eV or the bulk of the [Fe VII]-emitting region is shielded from this photoionizing continuum by intrinsic absorption.

6 SUMMARY AND CONCLUSIONS

We have used [Fe X] line emission to select a sample of galaxies from the SDSS with strong FHIL emission. The resulting 63 Seyfert galaxies comprise the first ever FHIL-selected sample of AGN. Moreover, it is the most homogeneous and one of the largest samples of FHIL-emitting galaxies to date. In each of these spectra, we have measured the strengths and profiles of several emission lines (including [Fe X], [Fe XI], [Fe VII], [O III] and Hα). We have also included soft X-ray data for all objects with available *ROSAT* measurements. From our analysis of these data, we conclude the following:

(i) That the [Fe X] and [Fe XI] lines are well correlated with both each other and the soft X-ray continuum flux, with a mean $[\mathrm{Fe\,X}]/F_{233-300\,\mathrm{eV}}$ ratio of 9.4×10^{-3}. Their correlation with the X-ray strength supports a photoionization origin of these line species, rather than collisional. The correlation with X-rays applies to all type 1 Seyferts and may be used to estimate soft X-ray fluxes based upon observed FHIL strengths.

(ii) There are significant differences in the [Fe X]/[Fe VII] ratios between NLS1s, BLS1s (including both 1.0 and intermediate type 1.5 Seyferts) and Sy2s, either because of selective absorption of the [Fe X] or because of a different ionizing continuum. In the Sy2s, the ratios of [Fe X]/[Fe VII] tend to be lower and the FWHM of the [Fe X] line profiles is narrower. These facts suggest that some fraction of the [Fe X] flux (i.e. the broad component) may be hidden in Sy2s, possibly because it is emitted in a region of size comparable to the dusty molecular torus. A subset of NLS1s has high [Fe X]/[Fe VII] and [Fe X]/[O III] ratios, which is consistent with an over production of [Fe X] in response to an excess of ionizing photons in the soft X-ray band.

(iii) Using the low-ionization lines of [S II] as a proxy for the systemic velocity of the host galaxy, we find that [Fe XI], [Fe X] and [Fe VII] are generally blueshifted with velocities of the order

[11] In addition to its extreme soft excess, KUG 1031+398 is of particular interest because the strongest evidence for a quasi-periodic oscillation in an AGN has recently been discovered in this object (Gierliński et al. 2008).

[12] Note that whilst this figure uses Hα_T, Hα_T is a reasonable proxy for Hα_B in type 1 Seyferts because the majority of the Hα flux is contributed by the broad component.

of 100 km s^{-1}. The most blueshifted lines tend to have the broadest profiles. In particular, about one-third of [Fe XI] lines are both broader and bluer than the other FHILs. The [O III] lines are found to have blue wings with widths and velocities comparable to those of the FHILs and narrow cores at the systemic velocity.

(iv) In our correlations, there are a few sources that consistently are far from the general trends. These outliers are type 1 Seyferts that have the narrowest Hα_B lines amongst our NLS1s and the softest X-ray spectra amongst our entire sample. Their deviations from the overall trends may be manifestations of important intrinsic differences between examples of very narrow-line BLRs and the majority of Sy1s.

(v) The good correlation between F_x and [Fe X] emission observed 10–15 years later means that the measured X-ray flux (an instantaneous snapshot) is relatively representative of average X-ray power to which the FHIL-emitting region responds. It follows that variability over time-scales ranging from that of the *ROSAT* exposure times to the lag time of the SDSS observations (several minutes to several years) is usually no more than a factor of a few.

These findings are consistent with a stratified wind model, in which outflowing photoionized clouds produce [Fe XI], [Fe X], [Fe VII] and possibly the wings of [O III]. The [Fe XI]- and [Fe X]-emitting clouds lie closest to the BLR at a scale comparable to the obscuring torus, which sometimes cover a significant fraction of these clouds in Sy2s. [Fe VII], in comparison to [Fe X] and [Fe XI], is found to correlate less well with F_x and better with [O III]; it is also apparently not affected when the [Fe X] emitting region is partially covered. These facts suggest that the [Fe VII]-emitting region is more extended and may approach the scale of the NLR. However, the correlation between [Fe VII] and [Fe X] fluxes and in particular the similarity of their velocity shifts implies that the clouds emitting these features are related to each other and may be different parts of the same outflow. The narrow cores of [O III] and the other low-ionization species, such as [O I], do not have a velocity shift relative to [S II]; the clouds emitting these lines are either a decelerated portion of the outflow or unrelated to it.

Based upon the strong correlation between [Fe X] and soft X-ray flux (Section 5.2) and our discussion of the sources that appear to be exceptions to the overall correlations found in the sample (Section 5.4), we infer that strong [Fe X] emission (relative to other optical lines such as [O III] and [Fe VII]) is an optical-wavelength indicator of strong soft excesses in the X-ray band. Furthermore, the fact that these same objects do not have high [Fe VII]/[O III] ratios suggests that either these soft excesses do not continue through $\sim$100 eV into the difficult-to-observe extreme ultraviolet band or the [Fe VII]-emitting clouds are shielded from the soft excess by intrinsic absorption. The connection between FHIL emission and the intrinsic continuum in the few hundred eV range needs to be tested with better X-ray data. A more detailed analysis of the available X-ray data would be useful, but the number of [Fe X]-selected sources with available X-ray spectra is severely limited. New observations would be necessary to better calibrate the FHIL–X-ray correlations.

Finally, we note that our [Fe X] selection yielded only one object that is not obviously an AGN (Source 45 here; Ward et al., in preparation). This confirms that it is exceptionally rare for non-active galaxies to produce strong FHIL emission. However, we cannot quantify just how rare this is (or what fraction of AGN are strong FHIL emitters, or whether one Seyfert class is more likely than another to have strong FHILs) because the present study does not include a control group. To remedy this, we are conducting a broader search for FHIL emission amongst a much larger sample of SDSS emission line galaxies. This next step will reduce selection effects in the present sample and will better enable us to put [Fe X]-selected sources into context.

ACKNOWLEDGMENTS

The authors wish to thank Matthew Boulton for his contributions in an early stage of this programme, and the anonymous referee whose suggestions helped to make this a stronger paper.

This research has made use of data obtained from the HEASARC, provided by NASA's Goddard Space Flight Center; NASA's Astrophysics Data System and the NASA/IPAC Extragalactic Data base, which is operated by the Jet Propulsion Laboratory, California Institute of Technology, under contract with the National Aeronautics and Space Administration.

Funding for the SDSS and SDSS-II has been provided by the Alfred P. Sloan Foundation, the participating institutions, the National Science Foundation, the US Department of Energy, the National Aeronautics and Space Administration, the Japanese Monbukagakusho, the Max Planck Society and the Higher Education Funding Council for England. The SDSS web site is http://www.sdss.org/. The SDSS is managed by the Astrophysical Research Consortium for the participating institutions. The participating institutions are the American Museum of Natural History, Astrophysical Institute Potsdam, University of Basel, University of Cambridge, Case Western Reserve University, University of Chicago, Drexel University, Fermilab, the Institute for Advanced Study, the Japan Participation Group, Johns Hopkins University, the Joint Institute for Nuclear Astrophysics, the Kavli Institute for Particle Astrophysics and Cosmology, the Korean Scientist Group, the Chinese Academy of Sciences (LAMOST), Los Alamos National Laboratory, the Max Planck Institute for Astronomy (MPIA), the Max Planck Institute for Astrophysics (MPA), New Mexico State University, Ohio State University, University of Pittsburgh, University of Portsmouth, Princeton University, the United States Naval Observatory and the University of Washington.

REFERENCES

Adelman-McCarthy J. K. et al., 2008, ApJS, 175, 297
Antonucci R., 1993, ARA&A, 31, 473
Appenzeller I., Öestreicher R., 1988, AJ, 95, 45
Baldwin J. A., Phillips M. M., Terlevich R., 1981, PASP, 93, 5
Barvainis R., 1987, ApJ, 320, 537
Becker R. H., White R. L., Helfand D. J., 1995, ApJ, 450, 559
Bennert N., Jungwiert B., Komossa S., Haas M., Chini R., 2006a, A&A, 459, 55
Bennert N., Jungwiert B., Komossa S., Haas M., Chini R., 2006b, A&A, 456, 953
Blustin A. J., Page M. J., Fuerst S. V., Branduardi-Raymont G., Ashton C. E., 2005, A&A, 431, 111
Boller T., 2000, New Astron. Rev., 44, 387
Condon J. J., Cotton W. D., Greisen E. W., Yin Q. F., Perley R. A., Taylor G. B., Broderick J. J., 1998, AJ, 115, 1693
De Robertis M. M., Osterbrock D. E., 1984, ApJ, 286, 171
De Robertis M. M., Osterbrock D. E., 1986, ApJ, 301, 727
Erkens U., Appenzeller I., Wagner S., 1997, A&A, 323, 707
Gierliński M., Middleton M., Ward M., Done C., 2008, Nat, 455, 369
Goodrich R. W., 1989, ApJ, 342, 224
Kraemer S. B., Schmitt H. R., Crenshaw D. M., 2008, ApJ, 679, 1128
Middleton M., Done C., Gierliński M., 2007, MNRAS, 381, 1426
Mullaney J. R., Ward M. J., 2008, MNRAS, 385, 53
Mullaney J. R., Ward M. J., Done C., Ferland G. J., Schurch N., 2009, MNRAS, 394, L16

Murayama T., Taniguchi Y., 1998, ApJ, 497, L9 (MT98)
Nagao T., Taniguchi Y., Murayama T., 2000, AJ, 119, 2605 (NTM00)
Oke J. B., Sargent W. L. W., 1968, ApJ, 151, 807
Osterbrock D. E., 1981, ApJ, 246, 696
Peterson B. M. et al., 2004, ApJ, 613, 682
Porquet D., Dumont A.-M., Collin S., Mouchet M., 1999, A&A, 341, 58
Puchnarewicz E. M., Mason K. O., Siemiginowska A., Fruscione A., Comastri A., Fiore F., Cagnoni I., 2001, ApJ, 550, 644
Rodríguez-Ardila A., Viegas S. M., Pastoriza M. G., Prato L., 2002, ApJ, 579, 214
Rodríguez-Ardila A., Prieto M. A., Viegas S., Gruenwald R., 2006, ApJ, 653, 1098
Spergel D. N. et al., 2003, ApJS, 148, 175
Stoughton C. et al., 2002, AJ, 123, 485
Suganuma M. et al., 2006, ApJ, 639, 46
Veilleux S., 1988, AJ, 95, 1695
Veilleux S., 1991, ApJS, 75, 383
Voges W. et al., 1999, A&A, 349, 389
Voges W. et al., 2000, IAU Circ. 7432, 3
White N. E., Giommi P., Angelini L., 2000, VizieR Online Data Catalog, IX, 31
York D. G. et al., 2000, AJ, 120, 1579
Zhang K., Wang T., Dong X., Lu H., 2008, ApJ, 685, L109
Zhou H., Wang T., Yuan W., Lu H., Dong X., Wang J., Lu Y., 2006, ApJS, 166, 128

APPENDIX A: ONLINE SUPPLEMENTARY MATERIAL

In Figs A1–A5, we plot various line luminosities against the luminosities of [O I] (Fig. A1), $[O\,III]_T$ (A2), $H\alpha_T$ (A3), [Fe X] (A4) and 0.1–2.4 keV X-rays (A5). In Tables A1–A6, we present the best-fitting line parameters for [Fe X] (Table A1), [Fe XI] (Table A2), [Fe VII] (Table A3), [O III] (Table A4), the lower ionization forbidden emission line doublets [O I] and [S II] (Table A5) and the Hα components (Table A6). In Table A7, we provide the compiled *ROSAT* data used in this study: count rates from the RASS (Voges et al. 1999, 2000) and the White et al. (2000) Catalogue of sources found in pointed *ROSAT* observations, RASS hardness ratios and flux estimates based upon these count rates. These figures and tables are provided online in their entirety.

SUPPORTING INFORMATION

Additional Supporting Information may be found in the online version of this article:

Figure A1. Luminosities of (a) $[O\,III]_T$, (b) $H\alpha_T$, (c) $[Fe\,VII]_T$ and (d) [Fe X] versus [O I]. Spectral classifications are indicated by point colours and styles as follows: NLS1 = cyan squares, Sy1.0 = blue circles, Sy1.5 = green triangles, Sy1.9 = magenta diamonds and Sy2 = red stars. The numbers in the lower-right corners are the mean of the log (line/[O I]) values, with the rms about this average ratio given in parentheses.

Figure A2. Luminosities of (a) [O I], (b) $H\alpha_T$, (c) $[Fe\,VII]_T$ and (d) [Fe X] versus $[O\,III]_T$. Spectral classifications are indicated as in Fig. A1 and the numbers are again the mean of the logarithmic ratios (this time over $[O\,III]_T$) and the rms about this average (in parentheses).

Figure A3. Luminosities of (a) [O I], (b) $[O\,III]_T$, (c) $[Fe\,VII]_T$ and (d) [Fe X] versus $H\alpha_T$. Sy2 sources are omitted because their $H\alpha_T$ luminosities are systematically lower because the broad component is not detected (see e.g. Fig. A2b). Apart from the lack of Sy2s, point styles identical to Fig. A1 and the numbers are again the mean of the logarithmic ratios (over $H\alpha_T$) and the rms about this average (in parentheses).

Figure A4. Luminosities of (a) [O I], (b) $[O\,III]_T$, (c) $H\alpha_T$, (d) $[Fe\,VII]_T$ and (e) [Fe XI] versus [Fe X]. Point styles as in Fig. A1 and the numbers are the mean of the logarithmic ratios (over [Fe X]) and the rms about this average (in parentheses).

Figure A5. Luminosities of (a) [O I], (b) $[O\,III]_T$, (c) $H\alpha_T$, (d) $[Fe\,VII]_T$ and (e) [Fe X] versus L_X in the 0.1–2.4 keV band. Point styles as in Fig. A1 and the numbers are again the mean of the logarithmic ratios (over F_x) and the rms about this average. The three Sy2s with *ROSAT* detections are omitted because they are likely to be affected by X-ray absorption.

Table A1. Best-fitting [Fe X] models.

Table A2. Best-fitting [Fe XI] models.

Table A3. Best-fitting [Fe VII] models.

Table A4. Best-fitting [O III] models.

Table A5. Best-fitting models for forbidden emission lines with lower IPs.

Table A6. The parameters of the narrow and broad components and the overall Hα models.

Table A7. *ROSAT* X-ray data.

Please note: Wiley-Blackwell are not responsible for the content or functionality of any supporting materials supplied by the authors. Any queries (other than missing material) should be directed to the corresponding author for the article.

This paper has been typeset from a TEX/LATEX file prepared by the author.